Coupling of multicomponent transport models in particle-resolved fluid-solid simulations

Chemical Engineering Science 291 (2024) 119920

Contents lists available at ScienceDirect

Chemical Engineering Science

journal homepage: www.elsevier.com/locate/ces

Coupling of multicomponent transport models in particle-resolved fluid-solid simulations

S. Tadayon Mousavi *, C.M.Y. Claassen, M.W. Baltussen, E.A.J.F. Peters, J.A.M. Kuipers

Chemical Engineering and Chemistry Department, Eindhoven University of Technology, Eindhoven 5600 MB, the Netherlands

ARTICLE INFO

Keywords:
Symmetric multicomponent transport modeling
Dusty Gas Model
Maxwell-Stefan equations
Immersed Boundary Method
Transport in porous media

ABSTRACT

An accurate and self-consistent methodology for mass transport of multi-component mixtures in multi phase media is a necessity for a proper description of complex physical and chemical processes in reactors such as catalytic packed beds. In this regard, a novel methodology has been developed to describe and couple underlying transport phenomena in fluid and porous media as well as at the solid-fluid interface. The methodology is symmetric as it treats all components in a mixture equally. The Maxwell-Stefan equations are symmetrically formulated, discretized conservatively and coupled with a compressible flow solver for the fluid part. The Dusty Gas Model is applied inside porous media by developing a self-consistent and robust numerical formulation. A ghost-cell Immersed Boundary Method is used to capture the physics at the solid-fluid interface with the implementation of a novel symmetric non-singular mass flux formulation. Several test cases are established to demonstrate the accuracy and robustness of the newly developed symmetric methodology in this paper. These test cases can be used as benchmark for the future development of symmetric methodologies for multicomponent systems in multi phase media.

1. Introduction

Global warming and the world's excessive demand of energy sources drive the need to invent or re-design many industrial processes with catalytic pellets such as the Fischer-Tropsch process. In order to achieve a more efficient operation, one should understand better:

- the interplay of transport phenomena with reactions inside the catalytic particles,
- the impact of hydrodynamics outside the catalytic pellets on
  - diffusion of reactants into particles as well as diffusion of products out of the pellets,
  - distribution of reactants and products inside the reactor.

Predictive mathematical models that are able to capture those phenomena accurately are helpful not only to understand and to recognize the dominant physical and chemical mechanisms inside as well as outside the catalytic pellets, but also to design an efficient reactor at a lower cost. Such a model is presented in this work for coupling of transport phenomena (convection and diffusion) inside and outside of a catalytic pellet.

The methodology presented in this paper is based on an Immersed Boundary Method (IBM) to demarcate inside of a particle from an outside medium. One of the main advantage of an Immersed Boundary Method is that there is no need to have a body fitted grid near moving or fixed objects in a fluid medium. Consequently, complex unstructured grids to capture the arbitrariness of an object and re-meshing in case of moving objects are unnecessary. In addition, a non-boundary fitted Cartesian computational grid requires less memory to store the grid information and avoids complicated processes to implement computationally efficient solvers for governing equations (Mittal and Iaccarino, 2005). There are a variety of IBM implementations for rigid and elastic bodies in literature. Mainly, they can be classified to three categories: the momentum forcing approach, the cut-cell finite volume approach, and the ghost cell approach (Das et al., 2017; Mittal and Iaccarino, 2005). In the momentum forcing approach, the no-slip condition is imposed by introducing a source term in the momentum equations at the immersed boundary. Calculation of a proper forcing term is the main challenge of this approach. Several methodologies are introduced in the literature to provide the desired accuracy and to avoid spurious oscillations to solve the Navier-Stockes equations over a broad range of Reynolds numbers. Some of those methodologies calculate and obtain a desired velocity at the immersed boundary in an iterative manner with a

* Corresponding author.
E-mail address: s.tadayon.mousavi@tue.nl (S. Tadayon Mousavi).

https://doi.org/10.1016/j.ces.2024.119920
Received 21 August 2023; Received in revised form 31 January 2024; Accepted 21 February 2024
Available online 28 February 2024

feedback loop (Goldstein et al., 1993; Peskin, 1972; Saiki and Biringen, 1996; Tang et al., 2014), while others introduced a direct approach to impose the forcing term in the momentum equations (Kempe and Fröhlich, 2012; Kim and Choi, 2006; Taira and Colonius, 2007; Tenneti et al., 2011; Uhlmann, 2005).

The cut-cell finite volume approach identifies the cells that are cut by the immersed boundary and changes the geometries of those cells in order to generate a body fitted Cartesian grid. It is claimed the local and global conservation of mass and momentum are enhanced in comparison with other methods because of the possibility to perform accurate flux calculations over the distorted faces of the cut cells in the vicinity of the fluid-solid interface (Cheny and Botella, 2010; Das et al., 2017; Mittal and Iaccarino, 2005; Ye et al., 1999). Extension of this method to 3D simulations with complex geometrical objects is cumbersome due to generation of complex cut cells and difficulty in properly discretization of governing equations for those cells (Das et al., 2017).

The ghost-cell Immersed Boundary Method, however, provides a more convenient approach to satisfy the no-slip boundary condition or other desired boundary conditions of governing equations on the immersed surface by forcing the condition via ghost cells (cells near to the immersed boundary) (Das et al., 2017; Deen et al., 2012; Mittal et al., 2008; Tseng and Ferziger, 2003). The ghost-cell immersed boundary method has been implemented before for applying the no slip boundary condition at the boundaries of objects in the Navier-Stokes equations (Das et al., 2017; Deen et al., 2012). In addition, an extended version of the ghost-cell IBM is applied successfully for simulation of the conjugate heat and mass transfer with the Fickian diffusion model in a packed bed reactor (Chandra et al., 2020). In this paper, the ghost-cell immersed boundary method is extended for solving multicomponent mixtures both inside and outside a catalytic pellet with more comprehensive diffusion models rather than Fick's law.

As diffusion is one of the main aspects of the described reactors physics, we aimed to develop robust and self-consistent formulations to capture this phenomenon inside and outside a catalytic pellet accurately.

Broadly, there are three different approaches to model diffusion phenomena in a multicomponent mixture. The Fickian diffusion model, the Maxwell-Stefan equations, and solving complete form of species momentum equation (not bulk or mass averaged momentum equation for a mixture) for each species involved in a mixture. Basically, the goal in a multicomponent simulation is to model the velocity of each species ($\vec{v}_i$) involved in a mixture accurately.

$$\vec{v}_i = \vec{V} + \vec{v}_{d_i}. \tag{1}$$

In the first two approaches, the velocity of each species is decomposed into the mass-averaged velocity ($\vec{V}$) and the diffusive velocity ($\vec{v}_{d_i}$), equation (1) (Kuo, 2005). Then, the role of the Fickian diffusion model or the Maxwell-Stefan equations is to predict the diffusive velocities. The mass averaged velocity is usually determined by the Navier-Stokes equations or estimated from other suitable analytical approaches for the investigated physics. However, in the third approach, the species momentum equations are solved, so $\vec{v}_i$ is obtained directly, and there is no need for division of the velocity to averaged and diffusive ones. There are advantages and costs (potential drawbacks) for each mentioned approach.

The simplest approach is the Fick diffusion model where the diffusive flux of the species i to the species j is connected linearly to the gradient of its mass fraction (Kuo, 2005).

$$\vec{J}_{d_i} = \rho_i \vec{v}_{d_i} = -\rho D_{ij} \nabla \omega_i, \tag{2}$$

where $\vec{J}_{d_i}$, ρ_i, ρ, D_{ij}, and ω_i represent the diffusive flux of species i, the mass density of species i, the mixture mass density, and the binary diffusion coefficient of species i and j, respectively. Although, the Fick model is computationally the cheapest, it is valid only for the specific cases (Krishna and Wesselingh, 1997):

- Binary mixtures,
- Diffusion of dilute species i into a media, where there is a dominant background species in the system,
- Or when all binary diffusion coefficients have the same value, so the diffusive flux constraint is satisfied (detailed explanation can be found in section 2).

In order to have physical results where the mass and the diffusive flux constraints are satisfied, body forces like the electromagnetic, the gravity, and the centrifugal force should be absent in a simulation where one of the above mentioned conditions is valid. Only under these conditions, the division of the species velocities to the mass averaged and the diffusive velocities can provide a consistent representation of a physical system with the Fickian model.

For modeling of multicomponent processes such as Fischer-Tropsch, specifying the dominant species is not possible, hence the Fickian diffusion does not provide a suitable option.

The second option is the Maxwell-Stefan (MS) equations, solving this set of equations provides solution for the diffusive velocities. These equations are derived by subtracting the non-conservative bulk momentum equation multiplied with a species mass fraction from the equation that is the result of subtraction of the species continuity equation multiplied by the species velocity from its momentum equation (Whitaker, 2009). More information about different forms of transport equations and their derivations, can be found in Tadayon Mousavi (2020). There is no restriction for the type and number of species present in a mixture. In addition, body forces are included. However, a couple of assumptions are made throughout the derivation of the Maxwell-Stefan equations (Whitaker, 2009):

- the governing equation for the diffusive velocity is quasi-steady,
- the diffusive inertial effects are negligible,
- the viscous effects (shear stress terms) are negligible,
- the effects of the homogeneous chemical reactions are negligible.

The final form of these equations for an ideal-gas mixture is (Krishna and Wesselingh, 1997; Taylor and Krishna, 1993; Whitaker, 2009):

$$-\nabla x_i - \underbrace{\frac{1}{p}(x_i - \omega_i)\nabla p}_{\text{pressure diffusion}} + \underbrace{\frac{\rho_i}{p}(\vec{F}_i - \sum_{j=1}^{N} \omega_j \vec{F}_j)}_{\text{forced diffusion}} =$$
$$\underbrace{\sum_{\substack{j=1 \\ j\neq i}}^{j=N} \frac{x_i x_j}{D_{ij}}(\vec{v}_{d_i} - \vec{v}_{d_j})}_{\substack{\text{inter molecular} \\ \text{friction force}}} + \underbrace{\sum_{\substack{j=1 \\ j\neq i}}^{N} \frac{x_i x_j}{D_{ij}}\left(\frac{D_i^T}{\rho_i} - \frac{D_j^T}{\rho_j}\right)}_{\text{thermal diffusion}}, \tag{3}$$

where x_i, p, $\vec{F}_i$, D_i^T represent the molar fraction of species i, pressure, body forces per unit of mass act on the species i, and the thermal diffusion of species i, respectively.

As mentioned above, in the derivation of the Maxwell-Stefan equations, it is assumed the shear is negligible. For situations that this assumption is not valid such as very narrow tubes, where the viscous shear force is more dominant than the friction force between different species, solving the momentum equations for each species involved in a mixture could provide more accurate results (Kerkhof and Geboers, 2005). In wide tubes, the velocity gradients are smaller. Therefore, the momentum exchange between different species, which homogenizes species velocities, dominants the momentum exchange between faster and slower regions of a tube for each species. Under this condition, a single momentum equation which represents the whole mixture, the bulk momentum equation, is computationally more efficient to solve than species momentum equations (Kerkhof and Geboers, 2005). Franců and Mikyška (2020) present a computational approach that follows this non-splitting species velocity in multicomponent mixtures in porous media. How-

ever, in general, this approach is computationally more expensive in comparison with the first two approaches.

In this research, for the fluid media outside a catalytic particle, the bulk momentum equation is solved to obtain the mass-averaged velocity. Then, the species mass balances coupled with the Maxwell-Stefan equations are solved to update the mixture composition. In the porous media where the "viscous shear" dominates the "diffusive friction", the Dusty Gas Model (DGM) (Krishna and Wesselingh, 1997; Mason Edward and Malinauskas, 1983) is chosen to model the transport phenomena instead of solving the species momentum equations; as we found the Dusty Gas Model computationally more feasible.

In addition, the developed formulations in this paper treat all N components of a mixture similarly, which is called the symmetric approach (Bothe and Druet, 2023; Giovangigli, 1990, 1991; Peerenboom et al., 2011). Conventional models (the asymmetric approach) solve governing equations for only *N-1* species and update the concentration or the mass fraction of N^{th} species by forcing the system's constraints. The main disadvantage of the asymmetric approach is the necessity to a priori choose a N^{th} component, which is problematic for chemical reactors simulations with complex mixtures. Complex kinetics are interwoven with transport phenomena in such reactors, so there is no guarantee that the species mass balance is conserved. The symmetric modeling provides an elegant approach to treat each involved species in a mixture as a separate unknown of the discretized governing equations (Bothe and Druet, 2023; Peerenboom et al., 2011). Hence, non-physical values for mass fractions or concentrations during a simulation are avoided with proven mathematical formulations, a proper discretization of governing equations and appropriate boundary conditions.

In the following sections, first we present a non-singular Maxwell-Stefan equations formulation coupled with a compressible flow solver. Then, the Maxwell-Stefan equations are extended to porous media, and our developed self-consistent Dusty Gas Model formulation is explained. In the last section, a novel non-singular formulation for the mass transfer at the boundary of solid-gas for multicomponent mixtures is developed. Furthermore, it is shown how this formulation can be implemented with the ghost-cell Immersed Boundary Method where the Maxwell-Stefan formulation is used for a medium outside a particle, and the DGM models transport physics inside a pellet.

2. Non-singular formulation of the Maxwell-Stefan equations and its coupling with a compressible flow solver

Continuity equations for each species involved in a mixture are solved coupled with a compressible flow solver in order to model hydrodynamics and the composition of a multicomponent medium. In this section, the continuity equations with the Maxwell-Stefan diffusive velocities are discussed first. Then, the implemented coupling approach with a compressible flow solver and the used discretization are explained. At the end, a verification test case is shown. It should be noted that we used mass non-conservative form of governing equations throughout the whole work rather than the concentration equations for species.

As discussed before, all N components involved in a mixture are treated as a separate unknown in the presented methodology. The species velocity $\vec{v}_i$ is decomposed into the mass-averaged and the diffusive velocity, equation (1), so the continuity equation for each species has the following form:

$$\frac{\partial\left(\rho\omega_i\right)}{\partial t}+\nabla\cdot\left(\rho\omega_i\vec{V}\right)+\nabla\cdot\left(\rho\omega_i\vec{v}_{d_i}\right)=r_i, \tag{4}$$

where r_i represents the species source term due to chemical reactions. Finite volume discretization is used in this research, where scalar fields are stored at the center of cell, and velocity fields at faces (the staggered grid). In order to avoid extrapolation of the bulk density (ρ, which is coupled with pressure, and both are stored in the center of cells) at faces as much as possible, the non-conservative form of the species continuity equation is used in our implementation

$$\rho\frac{\partial\omega_i}{\partial t}+\rho\nabla\cdot\left(\omega_i\vec{V}\right)-\rho\omega_i\nabla\cdot\vec{V}+\nabla\cdot\left(\rho\omega_i\vec{v}_{d_i}\right)=r_i. \tag{5}$$

As the species velocity is divided, and the diffusive velocities are defined with respect to the mass-averaged velocity, the system of equations have two constrains which are not satisfied automatically (Peerenboom et al., 2011; Tadayon Mousavi, 2020)

1. summation of diffusive fluxes should be zero

$$\sum_i\omega_i\vec{v}_{d_i}=0, \tag{6}$$

2. summation of mass fractions should be one

$$\sum_i\omega_i=1. \tag{7}$$

There is also another constraint which is imposed automatically by proper kinetic sets

$$\sum_i r_i=0, \tag{8}$$

which means the net produced mass by chemical reactions in a system is zero (Peerenboom et al., 2011; Tadayon Mousavi, 2020).

2.1. Numerical treatment of the Maxwell-Stefan equations

The diffusive velocities are modeled by the Maxwell-Stefan equations

$$\sum_{\substack{j=1\\ j\neq i}}^{j=N}\frac{x_ix_j}{D_{ij}}(\vec{v}_{d_i}-\vec{v}_{d_j})=-\nabla x_i. \tag{9}$$

It is assumed that the pressure diffusion, the forced diffusion and the thermal diffusion are negligible in this work, equation (3). If the above equation (9) is written in a matrix form, we obtain (Peerenboom et al., 2011)

$$\sum_j F_{ij}\vec{v}_{d_j}=-\nabla x_i, \tag{10}$$

where

$$F_{ij}=\begin{cases}\sum_{k\neq i}\frac{x_ix_k}{D_{ik}} & \text{if } i=j,\\ -\frac{x_ix_j}{D_{ij}} & \text{if } i\neq j.\end{cases} \tag{11}$$

Matrix $\mathbf{F}$ is singular as $\sum_j F_{ij}=0$ which means for a N components mixture, it is not possible to have N independent unknown diffusive velocities. Basically, there are $N-1$ independent equations, so either a system of $N-1$ equations should be solved, and the N^{th} component should be obtained via constraint 2, equation (7), or matrix $\mathbf{F}$ should be regularized. In this work, we chose regularization of matrix $\mathbf{F}$ following the works of Giovangigli (1990, 1991); Peerenboom et al. (2011) to avoid the selection of the N^{th} component.

The system's constraints are used for regularization of the Maxwell-Stefan equations. The species continuity equation (5) with the regularized diffusive flux matrix $\mathbf{\Gamma}$ is converted into the following form

$$\rho\frac{\partial\omega_i}{\partial t}+\rho\nabla\cdot\left(\omega_i\vec{V}\right)-\rho\omega_i\nabla\cdot\vec{V}+\nabla\cdot\left(\sum_j\Gamma_{ij}\nabla\omega_j\right)=r_i. \tag{12}$$

In the following sections, it is explained how these constraints are used to regularize both the left and the right hand sides of the Maxwell-Stefan equations (9) in order to construct a non-singular diffusive flux matrix.

2.1.1. Driving force of the Maxwell-Stefan equations: the mass fraction constraint

As is decided to use the mass form of the species continuity equations in this work, the right hand side of the Maxwell-Stefan equations (9) should be converted to the mass fraction form. The conversion of mole to mass fraction obeys the following relation (Kuo, 2005; Peerenboom et al., 2011)

$$x_i = \frac{M}{M_i}\omega_i, \tag{13}$$

and

$$\frac{1}{M} = \sum_j \frac{\omega_j}{M_j}, \tag{14}$$

where M and M_i stand for the molecular weight of a mixture and the species i, respectively. Then, the right hand side of equation (9) can be written as Peerenboom et al. (2011)

$$\nabla x_i = \frac{M}{M_i}\nabla\omega_i - M x_i \sum_j \frac{\nabla\omega_j}{M_j} = \sum_j M'_{ij}\nabla\omega_j. \tag{15}$$

The conversion matrix, $\mathbf{M'}$ is singular as $\sum_i M'_{ij} = 0$ (Peerenboom et al., 2011). As the matrix $\mathbf{M'}$ will be used to form the diffusive flux matrix $\mathbf{\Gamma}$, its singular nature makes the diffusive flux matrix also singular. The singular diffusive flux matrix produces ill-posed behavior in the formed matrices resulting from the set of discretized equations to be solved at each time step, with detrimental outcome for the numerical stability. In order to achieve unconditionally stable formulations, the matrix $\mathbf{M'}$ has to be regularized. Regularization follows the described approach in Giovangigli (1990); Peerenboom et al. (2011), which proceeds via the mass fraction constraint (7) in the conversion of mole to mass fraction relation (13)

$$x_i = \sigma\frac{M}{M_i}\omega_i, \tag{16}$$

with $\sigma = \sum_j \omega_j$. Now the right hand side of the Maxwell-Stefan equations (9) can be written as

$$\nabla x_i = \frac{M}{M_i}\omega_i\nabla\sigma + \frac{M}{M_i}\sigma\nabla\omega_i - M x_i \sum_j \frac{\nabla\omega_j}{M_j} = \sum_j \tilde{M}_{ij}\nabla\omega_j, \tag{17}$$

with the regularized matrix $\tilde{\mathbf{M}}$

$$\tilde{M}_{ij} = \begin{cases} \frac{M}{M_i}\left(\omega_i - x_i + \sigma\right) & \text{if } i = j, \\ M\left(\frac{\omega_i}{M_i} - \frac{x_j}{M_j}\right) & \text{if } i \neq j. \end{cases} \tag{18}$$

Now $\sum_i \tilde{M}_{ij} = 1$.

2.1.2. The diffusive velocity relation of the Maxwell-Stefan equations: the diffusive flux constraint

As clarified in section 2.1, the left hand side of the Maxwell-Stefan equations (9) is singular. The matrix $\mathbf{F}$ is regularized by imposing the diffusive flux constraint (6) following the proposed approach in Giovangigli (1990); Peerenboom et al. (2011).

$$\sum_j F_{ij}\vec{v}_{d_j} + \alpha\omega_i \sum_j \omega_j\vec{v}_{d_j} = -\sum_j \tilde{M}_{ij}\nabla\omega_j, \tag{19}$$

with α as a free parameter with the suggested form $\alpha = 1/\max\left(D_{ij}\right)$ (Giovangigli, 1991; Peerenboom et al., 2011). This approach actually produces an artificial diffusion term for the continuity equation of σ (imagine σ as a pseudo species and replace it instead of ω_i in equation (4)). Then, the conservative form of the σ continuity equation becomes elliptic, which guarantees $\sigma = 1$ at the whole numerical domain at all time steps if $\sigma = 1$ at all domain boundaries and the initial condition of a simulation (Giovangigli, 1990, 1991; Peerenboom et al., 2011). The regularized matrix $\tilde{\mathbf{F}}$ can be written now $\tilde{\mathbf{F}} = \mathbf{F} + \alpha\boldsymbol{\omega}\otimes\boldsymbol{\omega}$, where $\otimes$ represents the dyadic product between two vectors. Then, the Maxwell-Stefan diffusive velocities can be obtained as

$$\vec{v}_{d_i} = -\sum_j \tilde{F}^{-1}_{ij}\sum_j \tilde{M}_{ij}\nabla\omega_j. \tag{20}$$

Subsequently, the diffusive flux can be written as

$$\vec{J}_{d_i} = -\rho\omega_i\sum_j \tilde{F}^{-1}_{ij}\sum_j \tilde{M}_{ij}\nabla\omega_j. \tag{21}$$

Finally, the diffusive flux matrix $\mathbf{\Gamma} = \mathbf{R}\tilde{\mathbf{F}}^{-1}\tilde{\mathbf{M}}$, with $\mathbf{R} = \mathrm{diag}\left(\rho\omega_i\right)$. However, there is a possibility to formulate the Maxwell-Stefan equations in terms of the diffusive flux rather than the diffusive velocity, equation (10), (Peerenboom et al., 2011). We found that only the diffusive flux formulation is stable in our implementation. Therefore, we have

$$\sum_j H_{ij}\vec{J}_{d_j} = -\sum_j \tilde{M}_{ij}\nabla\omega_j. \tag{22}$$

The above equation is derived from (10) as follows

$$\sum_k\sum_j \underbrace{F_{ij}R^{-1}_{jk}}_{H_{ik}}\underbrace{R_{kj}\vec{v}_{d_j}}_{\vec{J}_k} = -\nabla x_i, \tag{23}$$

with the matrix $\mathbf{H}$ (Peerenboom et al., 2011)

$$H_{ij} = \begin{cases} \frac{\sigma M}{\rho M_i}\sum_{k\neq i}\frac{x_k}{D_{ik}} & \text{if } i = j, \\ -\frac{\sigma M}{\rho M_j}\frac{x_i}{D_{ij}} & \text{if } i \neq j. \end{cases} \tag{24}$$

Note that in the derivation of equation (24), the updated conversion equation (16) is used. The matrix $\mathbf{H}$ is also singular as $\sum_i H_{ij} = 0$, so regularization is needed. A suitable regularization can be derived as follows

$$\underbrace{\tilde{\mathbf{F}}\mathbf{R}^{-1}}_{\tilde{\mathbf{H}}} = \underbrace{\mathbf{F}\mathbf{R}^{-1}}_{\mathbf{H}} + \alpha\boldsymbol{\omega}\otimes\boldsymbol{\omega}\mathbf{R}^{-1}, \tag{25}$$

which results

$$\tilde{\mathbf{H}} = \mathbf{H} + \alpha'\boldsymbol{\omega}\otimes\boldsymbol{U}, \tag{26}$$

where $\boldsymbol{U} = [1,..,1]^T$ and $\alpha' = \alpha/\rho$. The obtained result for α' in this derivation corrected the diffusive flux formulation of the Maxwell-Stefan equations presented in Peerenboom et al. (2011) by replacing $\alpha = 1/\max\left(D_{ij}\right)$ with α' for regularization of the matrix $\mathbf{H}$. Now, the diffusive flux matrix is $\mathbf{\Gamma} = \tilde{\mathbf{H}}^{-1}\tilde{\mathbf{M}}$. Please note that the matrix $\mathbf{R}$ can be singular when one or more species mass fractions approach zero. However, the matrix $\tilde{\mathbf{H}}$ remains non-singular regardless of zero mass fractions for one or more components. Actually, it is the main reason for the unconditional stability for the diffusive flux formulation in our implementation.

2.2. Coupling of the species continuity equations with a compressible flow solver

In order to solve the species continuity equations (5), the mass averaged velocity ($\vec{V}$) and the bulk density (ρ) should be known. These two parameters together with the pressure field are obtained by a compressible flow solver. The bulk momentum equations that are solved in each time step of a simulation have the following form

$$\frac{\partial\left(\rho\vec{V}\right)}{\partial t} + \nabla\cdot\left(\rho\vec{V}\vec{V}\right) = -\nabla p + \nabla\cdot\tau, \tag{27}$$

where p and τ stand for pressure and the shear stress tensor

$$\tau = -\mu\left[\left(\nabla\vec{V}\right) + \left(\nabla\vec{V}\right)^T - \frac{2}{3}\left(\nabla\cdot\vec{V}\right)\mathbf{I}\right], \tag{28}$$

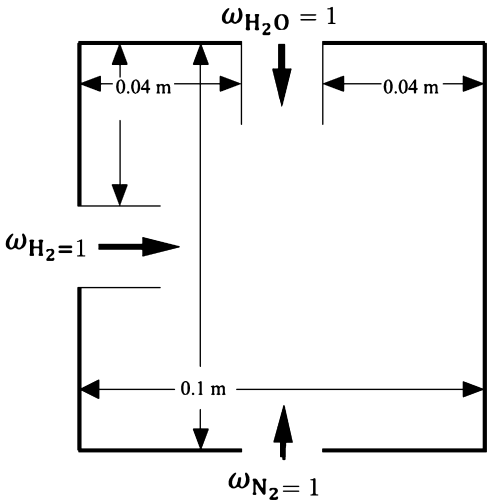

Fig. 1. Schematic of the verification test case for the Maxwell-Stefan equations coupled with the compressible flow solver (Peerenboom et al., 2011).

with μ and $\mathbf{I}$ as viscosity and the unity matrix. The finite volume approach is used to discretize the governing equations (5) and (27). All contributions to the momentum equations are treated explicitly, except the shear stress tensor. Only the diagonal components of the shear stress tensor are treated implicitly in this paper. The Upwind, the Central Difference (only for the species continuity equations and shear stress tensor terms), or Total Variation Diminishing (TVD) schemes are used for discretization of the convective fluxes (Versteeg and Malalasekera, 2007). The Min-Mod flux limiter is used in this research if TVD schemes are chosen for the discretization of the convective fluxes (Versteeg and Malalasekera, 2007).

The used flow solver in this research has a pressure-correction algorithm (Dijkhuizen, 2008), which is coupled with the ideal gas law to take into account the effect of compressibility due to composition changes. For each time step, first, the flow solver updates the velocity, the pressure, and the bulk density fields. The flow solver step requires a couple of iterations for each time step to satisfy the bulk continuity equation

$$\frac{\partial \rho}{\partial t} + \nabla \cdot \left(\rho \vec{V} \right) = 0. \tag{29}$$

Subsequently, the mixture composition is updated by solving the species continuity equations. At the end of each time step, the bulk density field is updated again by considering the new update for the composition. Appendix A describes the details of steps that are taken in each time step.

2.3. Verification test case

The 2D test case presented in Mazumder (2006); Peerenboom et al. (2011) is chosen to assess the formulation, the discretization and the implementation of the Maxwell-Stefan equations coupled with the compressible flow solver. The schematic of the domain and boundary conditions are depicted in Fig. 1. The test case provides a challenging scenario to test mass conservation in the implementation ($\sum_j \omega_j = 1$). Neumann boundary conditions are used for mass fractions in parts of the domain boundaries without specified values. Velocity is set zero at walls, and pressure is specified (1×10^5 Pa) for the boundary parts where one of the three species mass fraction is set to 1. Temperature is kept constant at 300 K during the simulation.

The grid resolution is 80×80. The binary diffusion coefficients that are used in this simulation are given in the Table 1.

Fig. 2 shows the comparison between the obtained results in this study with reproduction of the presented results in Peerenboom et al. (2011) by PLASIMO software (Plasimo, 2024; van Dijk et al., 2009), which is the in-house software of Peerenboom et al. (2011). Please note that, all three schemes: Upwind, Central Difference, and TVD are tried for the discretization of the convective fluxes. There is no difference between the results at steady-state. In addition, Fig. 3 shows a comparison of the obtained distribution of three mass fractions along 4 different lines in the numerical domain with PLASIMO software. The relative difference is less than 1%. Furthermore, $\sum_j \omega_j = 1$ is obtained up to the machine accuracy in our simulation.

Table 1
Used binary diffusion coefficients in the test case depicted in Fig. 2.

Species pair	Binary Diffusion Coefficient [m^2/s]
H_2O-H_2	8.8226×10^{-5}
H_2O-N_2	2.7471×10^{-5}
H_2-N_2	8.1374×10^{-5}

3. Extension of the Maxwell-Stefan equations to porous media: the Dusty Gas Model

In general gas transport through porous media involves four mechanisms (Kumar Das, 2019; Mason Edward and Malinauskas, 1983)

- Knudsen flow where the gas density is low, so the collisions between molecules can be ignored in comparison with the collisions between molecules and porous media walls.
- Continuum diffusion where different species of a mixture move relative to each other. The movements are driven by gradients of concentration, pressure, temperature (the thermal diffusion) and external forces. Molecule-molecule collisions dominate over molecule-wall collisions in this mode.
- Surface diffusion where molecules move along a solid surface in an adsorbed layer. This kind of transport is neglected in this study.
- Viscous flow where the gas acts as a continuum fluid medium and is driven by a pressure gradient. Molecule-molecule collisions dominate over molecular-wall collisions in this mode.

All the mentioned mechanisms can be combined in an analogy with an electrical circuit to depict the transport phenomena in a porous media. Fig. 4 shows this analogy. Each transport mode is represented by a resistor. The Knudsen diffusion and the continuum diffusion are resistors in series where the voltage drops are additive. However, the molecular diffusion branch is connected to the viscous flow and the surface diffusion in parallel where current is additive and voltage drop is the same (Mason Edward and Malinauskas, 1983).

The Dusty Gas Model (DGM) follows the same concept which is presented in Fig. 4 to describe transport in a porous media where the voltage drop and the electrical current resemble the pressure gradient and the flux, respectively. In addition, the porous media is considered as the $N + 1^{th}$ species (dust particles) of a mixture.

Basically, two independent transport modes resulting from the Chapman-Enskog kinetic theory (Ferziger and Kaper, 1973; Hirschfelder et al., 1964; Mason Edward and Malinauskas, 1983) are applied to a porous media where dust particles are treated as giant molecules. Hence, the Dusty Gas Model is comprised of: a diffusion part, consisting of a set of the Maxwell-Stefan equations, and a viscous-flow part, consisting of an equation for the bulk motion of a mixture (Mason Edward and Malinauskas, 1983). “Independent modes” means that there is not any direct coupling term due to diffusion in the bulk equation of motion, and no viscous momentum transfer term is seen in the diffusion equations explicitly. Therefore, these two transport mechanisms and their corresponding fluxes can be added simply (Mason Edward

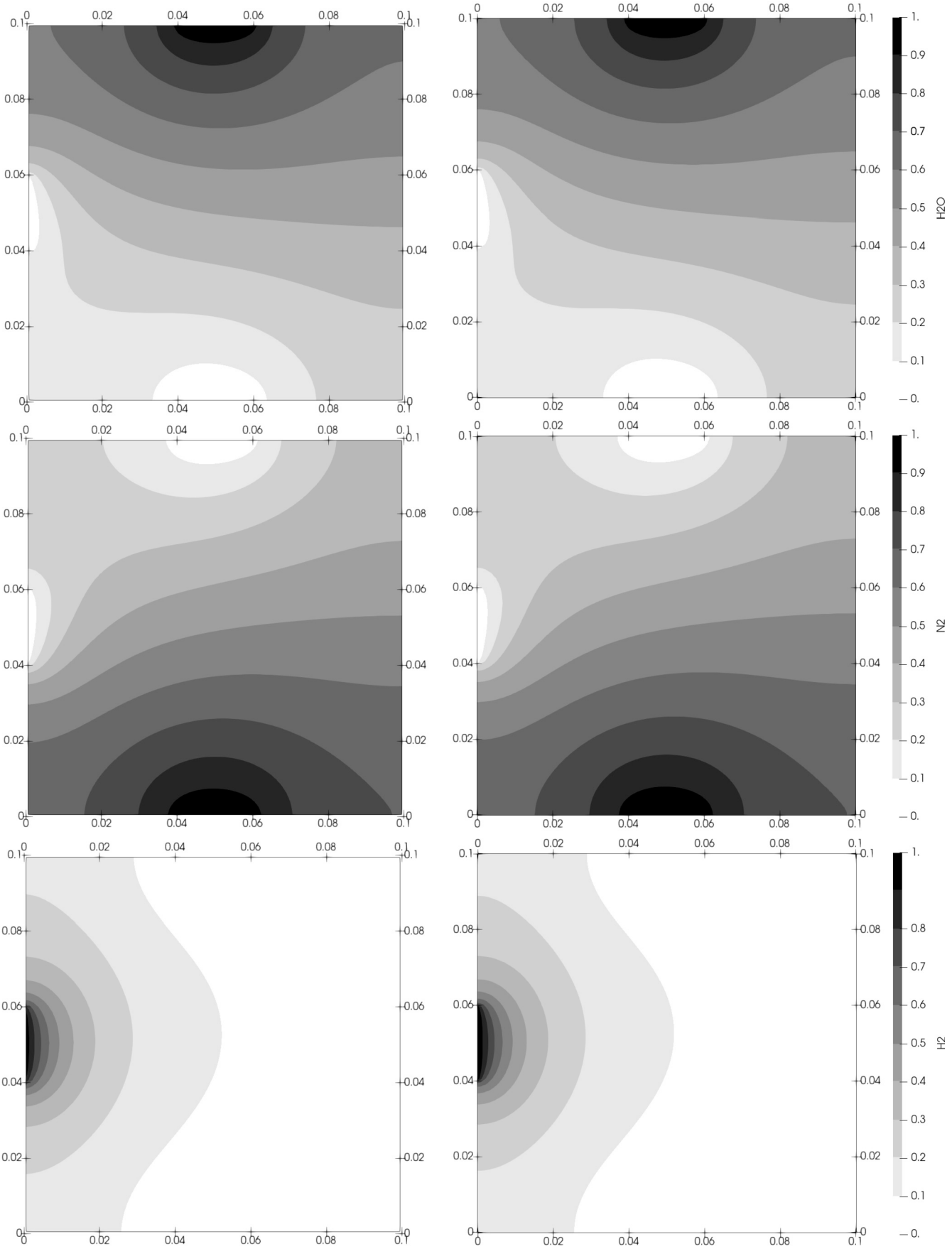

Fig. 2. The Maxwell Stefan diffusion simulation for a three species H_2O, H_2 and N_2 system for the depicted test case in Fig. 1. The right column are pictures of the reproduced results in Peerenboom et al. work (Peerenboom et al., 2011) by PLASIMO software, and the left column are obtained results in this study.

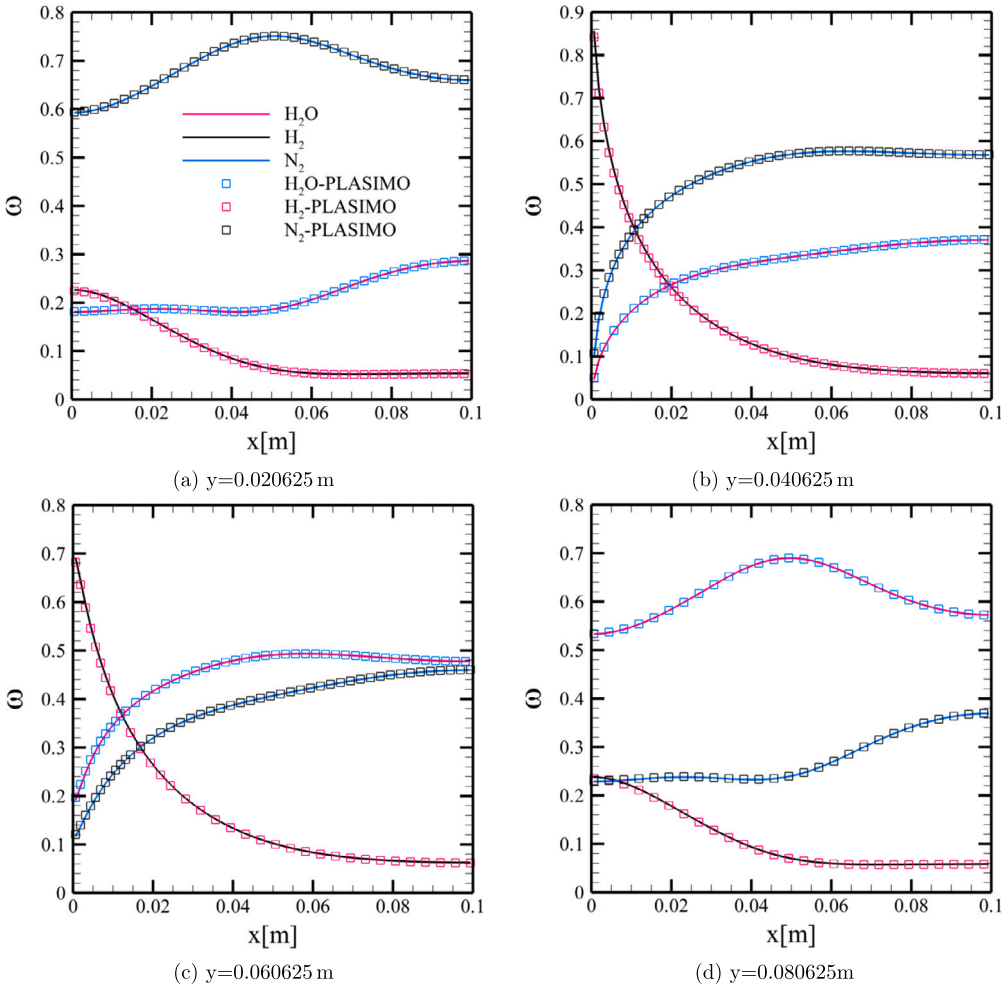

Fig. 3. The comparison of the distribution of mass fractions over 4 different lines in the numerical domain with the reproduced results in Peerenboom et al. work (Peerenboom et al., 2011) by PLASIMO software for the test case depicted in section 2.3.

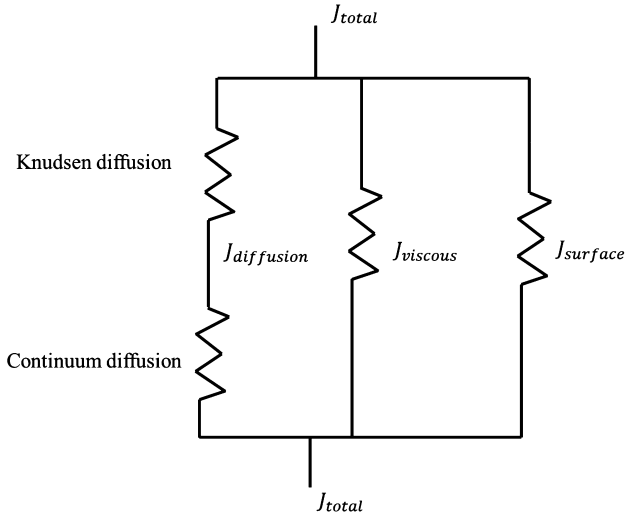

Fig. 4. Transport phenomena in a porous media in analogy with an electrical circuit (Mason Edward and Malinauskas, 1983).

and Malinauskas, 1983). Further information about assumptions, justifications, and the derivation of the Dusty Gas Model can be found in Mason Edward and Malinauskas (1983).

The final form of the Dusty Gas Model is

$$\sum_{\substack{j=1\\ j\neq i}}^{j=N} \underbrace{\frac{x_j x_i \vec{v}_i - x_i x_j \vec{v}_j}{D^e_{ij}}}_{\text{the Maxwell-Stefan equations}} + \underbrace{\frac{x_i}{D_{iK}}\vec{v}_i}_{\text{Knudsen flow}} + \underbrace{\frac{x_i}{D_{iK}}\frac{B_0}{\mu}\nabla p}_{\text{Viscous flow}} = \underbrace{-\nabla x_i - \frac{x_i}{p}\nabla p}_{\text{Driving force of continuum diffusion}}, \tag{30}$$

where the second term of "driving force of continuum diffusion" on the right hand side of equation (30) is the remaining part of "pressure diffusion" term of the general form of the Maxwell-Stefan equation (3). The rest of the "pressure diffusion" term is canceled out with some part of the "forced diffusion" term of (3) by applying the following assumption "the dust particles are held motionless by an external force which balances any pressure gradients in the gas" (Mason Edward and Malinauskas, 1983).

D^e_{ij} and D_{iK} represent the effective binary diffusion coefficient and the Knudsen diffusion coefficient in equation (30), respectively.

$$D^e_{ij} = \frac{\varepsilon}{\tau} D_{ij}, \tag{31}$$

with ε/τ as porosity-tortuosity factor of a porous medium. The Knudsen diffusion coefficient is calculated by

$$D_{iK} = \frac{\varepsilon}{\tau}\frac{d_0}{3}\left[\frac{8R_u T}{\pi M_i}\right]^{1/2}, \tag{32}$$

where d_0 represents the diameter of a pore (Krishna and Wesselingh, 1997; Kumar Das, 2019). In addition, B_0 in the final DGM formula (30) is a characteristic of a pore geometry.

3.1. Numerical treatment of the Dusty Gas Model

The Dusty Gas Model, equation (30), can be written in a matrix form similar to the Maxwell-Stefan equations as follows

$$\sum_j F'_{ij}\vec{v}_j = -\vec{d}_i, \tag{33}$$

where

$$F'_{ij} = \begin{cases} \sum_{l\neq i} \frac{x_i x_l}{D^e_{il}} + \frac{x_i}{D_{iK}} & \text{if } i = j, \\ -\frac{x_i x_j}{D^e_{ij}} & \text{if } i \neq j. \end{cases} \tag{34}$$

Contrary to the matrix $\mathbf{F}$ of the Maxwell-Stefan equations, equation (11), the matrix $\mathbf{F'}$ is not a singular matrix as $\sum_j F'_{ij} = x_i/D_{iK}$. Hence, it is not necessary to regularize $\mathbf{F'}$. Adding "dust particles" as the $N+1^{th}$ component of a mixture with the assumption that this component has zero flux regularizes automatically the left hand side of the Dusty Gas Model. The right hand side of Dusty Gas Model (33) is

$$\vec{d}_i = \nabla x_i + \frac{x_i}{p}\nabla p + \frac{x_i}{D_{iK}}\frac{B_0}{\mu}\nabla p. \tag{35}$$

Since we adopted the mass form of the species continuity equations, the Dusty Gas Model should be written in terms of mass fractions or species densities. Following a similar approach used for the Maxwell-Stefan equations, the Dusty Gas Model can be written in the mass fraction form by conversion of molar fraction to mass fraction gradient with the help of the conversion matrix $\tilde{\mathbf{M}}$, equation (18). The Dusty Gas Model can be written in the flux form in a similar way as described by equations (22) and (23) for the Maxwell-Stefan equations

$$\sum_j H'_{ij}\vec{J}_j = -\sum_j \tilde{M}_{ij}\nabla\omega_j - S_i, \tag{36}$$

where the matrix $\mathbf{H'}$ is $\mathbf{F'R^{-1}}$ with $\mathbf{R} = \mathrm{diag}\left(\rho\omega_i\right)$.

$$H'_{ij} = \begin{cases} \sum_{l\neq i} \frac{\sigma M}{\rho M_i}\left(\frac{x_l}{D^e_{il}}\right) + \frac{\sigma M}{\rho M_i D_{iK}} & \text{if } \quad i = j, \\ -\frac{\sigma M}{\rho M_j}\frac{x_i}{D^e_{ij}} & \text{if } \quad i \neq j. \end{cases} \tag{37}$$

Note that as $\mathbf{F'}$ is a non-singular matrix, although $\mathbf{R}$ can be singular when one or more mass fractions approach zero, $\mathbf{H'}$ is non-singular as $\sum_i H'_{ij} = \frac{\sigma M}{\rho M_i D_{iK}}$. Then, no regularization is needed for $\mathbf{H'}$ contrary to the matrix $\mathbf{H}$ of the Maxwell-Stefan equations (24). In addition, S_i is comprised of pressure gradient terms

$$S_i = \sigma\frac{M}{M_i}\omega_i\frac{\nabla p}{p} + \sigma\frac{M}{M_i D_{iK}}\omega_i\frac{B_0}{\mu}\nabla p. \tag{38}$$

In the above equation, the mole fraction is converted to the mass fraction with the help of equation (16). Then, the total flux for species i can be written as

$$\vec{J}_i = \sum_j \left(-\Gamma'_{ij}\nabla\omega_j - H'^{-1}_{ij}S_j\right), \tag{39}$$

where $\mathbf{\Gamma'} = \mathbf{H'^{-1}}\tilde{\mathbf{M}}$.

The described formulation of Dusty Gas Model is tested for cases with and without pressure gradient, these cases are explained in sections 3.2.1 and 3.2.2. The second term of equation (39) is taken into account explicitly which means that the gradient of pressure and consequently S_i are calculated by variables from the previous time step or iteration of a model. Note that all small matrices like $\mathbf{\Gamma}$ and $\mathbf{\Gamma'}$ are calculated based on the variables from the previous time step or iteration in this study. In addition, the pressure is calculated from the ideal gas law.

Unfortunately, we found that the mass fraction formulation of Dusty Gas Model with explicit source term is only stable for cases where there is no pressure gradient imposed. Even for those cases, an Under Relaxation Factor (URF) is needed to obtain physical and correct results. It should be noted that when the URF is used, first, a matrix system of discretized equations over the numerical domain is solved. Subsequently, the updated unknown variables (x^{n+1}) are not immediately used for calculations of the next iteration or the time step of a model. Only a fractional amount is added: $x^{n+1} = \mathrm{URF}x^{n+1} + (1-\mathrm{URF})x^n$, where URF is always a number in the range $[0, 1]$.

After trying extensively different formulations with explicit and implicit terms for conditions with and without pressure gradients. We found that a fractional step approach for composition and pressure for the Dusty Gas Model did not give a stable numerical scheme. We achieved only one formulation that guarantees physical and accurate results under any conditions without the need for an URF. The unconditional stable formulation of the Dusty Gas Model is density based where both mass fractions and pressure are expressed in terms of species mass densities. Appendix B presents the derivation of the newly formed Dusty Gas Model. The species continuity equations and consequentially the new formulation of the Dusty Gas Model flux are written as

$$\frac{\partial\rho_i}{\partial t} - \nabla\cdot\left(\sum_j \tilde{\Gamma}'_{ij}\nabla\rho_j\right) = r_i, \tag{40}$$

where

$$\tilde{\Gamma}'_{ij} = \frac{\Gamma'_{ij}}{\rho} - \sum_k \frac{\Gamma'_{ik}}{\rho^2}\rho_k + \frac{1}{M_j}\sum_k H'^{-1}_{ik}s_{1_k} + \frac{1}{M_j}\sum_k H'^{-1}_{ik}s_{2_k}, \tag{41}$$

with

$$s_{1_i} = \frac{\sigma M}{M_i}\frac{\rho_i}{\rho}\frac{R_u T}{p},$$
$$s_{2_i} = \frac{\sigma M}{M_i D_{iK}}\frac{\rho_i}{\rho}\frac{B_0}{\mu}R_u T. \tag{42}$$

R_u represents the universal gas constant. The species continuity equation, equation (40), is discretized in a similar way as the continuity equations with the Maxwell-Stefan diffusive fluxes. For the spatial part, the central difference is used where gradients of species mass densities are implicit whereas $\tilde{\mathbf{\Gamma}}'$ is calculated explicitly. If a simulation is time-dependent; then, a simple forward Euler scheme is implemented for the discretization of the temporal term. In the developed formulation, the pressure is calculated self-consistently with species mass densities, and there is no need for a flow solver as the total flux of species is captured by the Dusty Gas Model formulation directly.

3.2. Verification test cases

In order to verify the developed self-consistent formulation of the Dusty Gas Model, two test cases are implemented. In the first test case, no gradient of pressure is imposed over the numerical domain, while the robustness of the Dusty Gas Model formulation is tested for conditions with a pressure gradient in the second case.

3.2.1. Isobaric test case

For this test case, the experiment of Remick and Geankoplis (1974) is chosen to be mimiced numerically. In the experimental setup, 644 capillaries tubes with averaged inner diameter 0.00391 cm (pore diameter) and 0.96 cm length are installed in a diffusion cell. The molar fractions of a mixture of ternary species He, Ne, and Ar are kept constant at the two ends of tubes. In addition, the pressure and the temperature are also kept constant in the system. The experiments are performed at different pressures in order to cover the entire range of diffusion from Knudsen to Continuum diffusion, which means the transition region is

Table 2
Experimental test cases of Remick and Geankoplis work (Remick and Geankoplis, 1974).

No.	p [Pa]	Temp [°C]	x_{He_0}	x_{He_L}	x_{Ne_0}	x_{Ne_L}
1	59.99	27.6	0.0472	0.9471	0.5241	0.0343
2	146.655	28.3	0.0652	0.9610	0.5099	0.0251
3	545.2886	27.2	0.0572	0.9619	0.5134	0.0244
4	3021.0853	27.8	0.0622	0.9625	0.5102	0.0237
5	40422.0146	27.5	0.0539	0.9601	0.5051	0.0252

tested. After the system reaches steady-state for each experiment, the fluxes for each species are measured.

In our numerical test case, we solved the following equation

$$-\nabla \cdot \left(\sum_j \tilde{\Gamma}'_{ij} \nabla \rho_j \right) = 0. \tag{43}$$

Furthermore, the binary diffusion coefficients are calculated by the correlation represented by Fuller et al. (1966); Kumar Das (2019)

$$D_{ij} = \frac{10^{-7} T^{1.75} \left(\frac{1}{M_i} + \frac{1}{M_j} \right)^{0.5}}{p \left[\left(\sum V_i \right)^{\frac{1}{3}} + \left(\sum V_j \right)^{\frac{1}{3}} \right]^2}, \tag{44}$$

with p in [atm], T in [K], and D_{ij} in [m^2/s]. $\sum_i V_i$ represents the sum of diffusion volumes (Fuller et al., 1966). Diffusion volumes are 2.88, 5.59, and 16.1, for He, Ne, and Ar, respectively (Fuller et al., 1966; Kumar Das, 2019). The porosity-tortuosity (ε/τ) factor is set to 1 as we are dealing with straight tubes. The details of the five experimental test cases of Remick and Geankoplis work (Remick and Geankoplis, 1974) are listed in Table 2. Table 3 shows the comparison of fluxes between experiments and the obtained numerical results in this study.

As is clear, the numerical results capture the experimental values very well. The density based formulation of Dusty Gas Model, equation (43), is used to capture the physics in these test cases. Note that for the mass fraction based formulation of Dusty Gas Model, models could reach steady state and produce physical results, but an URF was needed for all test cases. For the density-based solution used here no under-relaxation was needed.

3.2.2. Non-isobaric test case

In order to assess the robustness of the developed formulation for the Dusty Gas Model, test cases where a pressure gradient is imposed over the numerical domain boundaries are tried. In this type of tests, next to different kinds of diffusion, the convective flux plays a significant role due to gradients of pressures. These cases were inspired by the experiments of Veldsink et al. (1994) for catalytic membranes. They imposed different gradients of pressure with various fixed molar fractions of a ternary mixture (N_2, Ar, He) over the two ends of a membrane. Then, the fluxes of species were measured after the steady-state condition was achieved. Unfortunately, the experimental test cases cannot be used directly as the summation of imposed molar fractions at the two ends of the membrane is higher than one for most test cases. In this study, the same gradient of pressure was imposed, but the compositions differ somewhat from those reported in Veldsink et al. (1994). Table 4 described the test cases that are used in this study.

Temperature is fixed at 298 K for all test cases. ε/τ, B_0, and μ are 0.147, 4.79×10^{-14} [m^2], 2.011×10^{-5} [Pa.s], respectively. The pore diameter is set to 34.8363×10^{-7} [m]. The binary diffusion coefficients are listed in Table 5. 100 grid points are used along the membrane.

Table 6 presents obtained fluxes in this study. Note that, no URF is needed for any test case with the density based formulation of the Dusty Gas Model. The mass fraction based formulation is not stable for cases with pressure gradients, and nonphysical results (negative mass fractions or mass fractions bigger than one) are produced even if URF is employed. The reported results in Table 6 are obtained by setting the residual criteria of the used in-house matrix solver equal to 1×10^{-13}. Please note that the residual is defined as the maximum absolute value difference of the new unknowns (in this case the species densities) to the old ones over the whole numerical domain.

4. Coupled mass transfer

At this stage, we have robust and conservative formulations for describing transport of multicomponent systems both in fluid and porous media. Our scheme will be completed by capturing the mass transfer physics at the interface of the fluid and the porous medium. In this regard, the ghost-cell Immersed Boundary Method (IBM) which is used to demarcate fluid from solid and the implementation of the developed symmetric non-singular mass flux formulation embedded in the IBM are discussed in detail in this section.

4.1. Immersed Boundary Method description

In this research, the ghost cell Immersed Boundary Method (Deen et al., 2012) is used to force desired conditions at the fluid-solid interface. Basically, the coefficients of unknown variables in the discretized representation of the governing equations are modified in such a way that imposed conditions at an immersed boundary (interface) are satisfied. In general, a discretized equation for each numerical cell (c) can be written in the following form

$$a_c \phi_c + \sum_{nb} a_{nb} \phi_{nb} = b_c, \tag{45}$$

with ϕ as an unknown variable. "nb" represents the index of all neighboring cells of a cell c. a_c and a_{nb} in equation (45) are the implicit part, and b_c is the explicit part of the system of equations. Imposing a proper boundary condition at the interface results in the values for the unknown variables at the immersed boundary. These values are treated as Dirichlet boundary condition at each intersect of fluid-solid. Corresponding coefficients and the right hand side of equation (45) for each cell that is located at the interface of fluid-solid are modified in order to satisfy those Dirichlet values at the interface (Das et al., 2017; Deen et al., 2012).

Fig. 5 depicts a numerical domain containing an arbitrary object. Consider a discretized equation which is solved for cell C_f whose center is located in the fluid part. This cell has intersects at "west" and "south" because the center of the west and the south neighbor cells are located in the solid phase. ϕ_b represents the value of a primary variable at the interface relevant for cell C_f. This value either is calculated by a proper immersed boundary condition or is set as a Dirichlet value.

Although this description focuses on the x-direction, the same approach is applied for other directions. C_s, the west neighbor cell of C_f is in the solid particle. Then, ϕ_{C_s} should be replaced based on fluid cells and the interface value (ϕ_b). In other words, the discretized coefficients (45) for each cell should be based on the values at the immersed boundary and cells at the same phase.

This can be achieved by using a second order fit ($\phi = ax^2 + bx + c$) for the value of the unknown at the solid part. ξ in Fig. 5 is a dimensionless distance between C_s and the immersed boundary. In the case of the x-direction Δx is used to make the distance dimensionless. Then, the following equation is obtained for ϕ_{C_s}

$$\phi_{C_s} = -\frac{2\xi}{1-\xi}\phi_{C_f} + \frac{\xi}{2-\xi}\phi_{C_{fE}} + \frac{2}{(1-\xi)(2-\xi)}\phi_b. \tag{46}$$

Subsequently, the coefficients of the left hand side and right hand side of equation (45) for cell C_f should be modified as follows

$$a_{C_f} = a_{C_f} - a_{C_s}\frac{2\xi}{1-\xi},$$

Table 3
Comparison of experimental versus numerical fluxes for the experimental test cases of Remick and Geankoplis work (Remick and Geankoplis, 1974). Fluxes are in [mol/cm^2/s].

No.	$N_{He_{exp}}$	$N_{He_{Num}}$	$N_{Ne_{exp}}$	$N_{Ne_{Num}}$	$N_{Ar_{exp}}$	$N_{Ar_{Num}}$
1	-3.733×10^{-6}	-3.4469×10^{-6}	1.100×10^{-6}	8.3829×10^{-7}	0.5966×10^{-6}	4.9523×10^{-7}
2	-6.810×10^{-6}	-7.656×10^{-6}	1.923×10^{-6}	1.8586×10^{-6}	1.06560×10^{-6}	1.1024×10^{-6}
3	-1.998×10^{-5}	-2.05963×10^{-5}	5.064×10^{-6}	5.0515×10^{-6}	2.843×10^{-6}	2.9291×10^{-6}
4	-4.414×10^{-5}	-4.18487×10^{-5}	9.437×10^{-6}	1.04424×10^{-5}	5.495×10^{-6}	5.8245×10^{-6}
5	-4.925×10^{-5}	-5.34454×10^{-5}	1.281×10^{-5}	1.32004×10^{-5}	7.472×10^{-6}	7.5354×10^{-6}

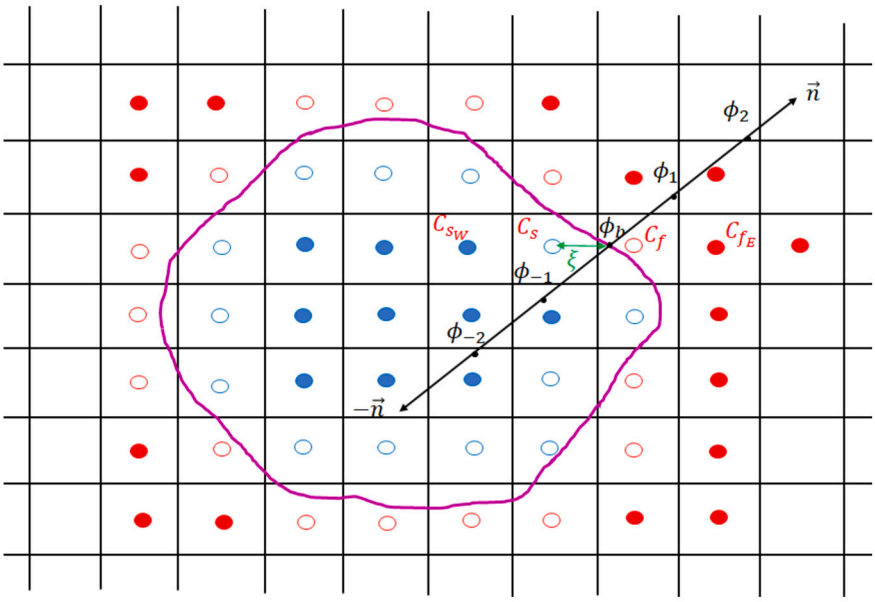

Fig. 5. An arbitrary immersed object in a numerical domain (Das, 2017). The blue and red circles are designated the center of cells which are located in the solid and the fluid parts, respectively. Hallow circles present cells which have at least one neighbor cell at a different phase. Solid circles present cells which do not have any intersect (all of their neighbor cells are in the same phase as their center).

Table 4
The used conditions over a membrane in this paper.

No.	p_L [Pa]	p_0 [Pa]	$x_{N_{2_0}}$	x_{Ar_0}	$x_{N_{2_L}}$	x_{Ar_L}
1	120000	132399.0	0.2862	0.4082	0.1975	0.5951
2		104134.6	0.6202	0.1798	0.5212	0.1190
3		123066.41	0.6657	0.1503	0.3640	0.3507
4		130665.8	0.6871	0.1341	0.3395	0.3805
5	200000.0	200399.967	0.7211	0.1056	0.4485	0.2261
6		210665.8	0.8225	0.1762	0.5126	0.1331
7		190267.47	0.6212	0.0432	0.3575	0.3590
8	300000.0	294000.49	0.6302	0.1685	0.5028	0.1481
9		300933.257	0.7331	0.0969	0.4330	0.2493
10		304132.99	0.7725	0.0714	0.3993	0.2975

Table 5
The used binary diffusion coefficients used for the test cases described in Table 4.

Species pair	Binary Diffusion Coefficient [m^2/s]
N_2-Ar	1.95×10^{-5}
N_2-He	7.072×10^{-5}
Ar-He	7.355×10^{-5}

Table 6
Numerical fluxes for the described conditions in Table 4. Fluxes are in [mol/m^2/s].

No.	N_{N_2}	N_{Ar}	N_{He}
1	0.142067	0.202217	0.156052
2	-0.311059	-0.0708484	-0.219876
3	0.080782	0.0165542	0.0132024
4	0.283545	0.0552432	0.0732066
5	0.0354218	-0.0033915	-0.0297428
6	0.477066	0.102133	-0.0126445
7	-0.191801	-0.192472	-0.151496
8	-0.248623	-0.0731846	-0.198836
9	0.0810427	-0.00139196	-0.0327865
10	0.265559	0.0218528	0.0238291

$$a_{C_{f_E}} = a_{C_{f_E}} + a_{C_s}\frac{\xi}{2-\xi},$$
$$b_{C_f} = b_{C_f} - a_{C_s}\frac{2}{(1-\xi)(2-\xi)}\phi_b,$$
$$a_{C_s} = 0. \tag{47}$$

This treatment is applied for all cells in both phases with intersects in all directions (x, y, z) after the value of primary variables are known at the immersed boundary (Chandra et al., 2020; Das, 2017; Das et al., 2017; Deen et al., 2012). It should be noted that when the immersed

boundary is very close to the center of cell, C_f, i.e. $\xi > 0.95$, the second order fit, equation (46), merges to infinity, so a first order fit is used in which the contribution of center of cell, ϕ_{C_f}, is not taken into account.

4.2. Coupled mass transfer formulation embedded in the Immersed Boundary Method

In order to describe the coupling of the mass transfer between solid porous particles and a fluid medium, the continuity of mass flux is enforced in the normal direction for each fluid-solid intersect. For a fluid medium, the Maxwell-Stefan equations together with a compressible flow solver are used. For a solid porous particle, the density-based formulation of the Dusty Gas Model is implemented. It should be noted that, one of the challenges that should be tackled to satisfy properly the continuity of mass flux, equation (48), is to choose a suitable primary variable for the species continuity equations.

$$\rho_{b_i} V_{b_n} - \sum_j \Gamma_{b_{ij}} \frac{\partial \omega_j}{\partial n}\Big|_{b_f} = - \sum_j \tilde{\Gamma}'_{b_{ij}} \frac{\partial \rho_j}{\partial n}\Big|_{b_s}. \tag{48}$$

Regarding continuity of flux in the normal direction equation (48), "n" represents the normal direction, Fig. 5. The subscripts "b", "f", and "s" stand for the values at an immersed boundary, a fluid medium, and a solid particle, respectively. $\mathbf{\Gamma}$ is the diffusive flux matrix of the Maxwell-Stefan equations, and $\tilde{\mathbf{\Gamma}}'$ is the self-consistent flux matrix of the Dusty Gas Model. V_{b_n} represents the fluid convective velocity perpendicular to a porous particle surface. V_{b_n} is usually considered zero (no-slip condition) at a solid particle surface. However, it can have a very small value for porous particles, but it does not need to be exactly zero. This matter will be discussed further later.

To solve the continuity of flux at the interface, we need to aim for one primary variable. It means either the Maxwell-Stefan equations should be written in a density-based form, or the Dusty Gas Model should be converted into a mass fraction based form. As discussed in section 3.1 extensively, the mass fraction based formulation of the Dusty Gas Model is not unconditionally stable, so the Maxwell-Stefan equations should be rewritten in a density-based form. Then, similar to the Dusty Gas Model and equation (B.2), we have for the Maxwell-Stefan equations

$$-\sum_j \Gamma_{ij} \nabla \omega_j = -\sum_j \Gamma_{ij} \frac{\nabla \rho_j}{\rho} + \sum_j \Gamma_{ij} \frac{\rho_j}{\rho^2} \nabla \sum_k \rho_k = -\sum_j \Gamma''_{ij} \nabla \rho_j. \tag{49}$$

The new matrix $\mathbf{\Gamma''}$ is singular unfortunately, as it is a product of a non-singular matrix $\mathbf{\Gamma}$ and a singular one $\mathbf{C}$, $\mathbf{\Gamma''} = \mathbf{\Gamma C}$. Matrix $\mathbf{C}$ is

$$C_{ij} = \begin{cases} \frac{1}{\rho} - \frac{\rho_i}{\rho^2} & \text{if } i = j, \\ -\frac{\rho_i}{\rho^2} & \text{if } i \neq j. \end{cases} \tag{50}$$

It is singular as $\sum_i C_{ij} = 0$. The source of singularity is hidden in the matrix, which is responsible to convert ∇x_i to $\nabla \rho_i$. Several attempts were made to regularize the density-based formulation of the Maxwell-Stefan model, like dividing the conversion matrix of ∇x_i to $\nabla \rho_i$ to a non-singular matrix and a source term. However, none of them proved to provide an unconditionally stable formulation as singularity is not cured, but its form is only changed. Our conclusion is that regularization of the Maxwell-Stefan equations should be done by either using a system constraint (like in the mass fraction based Maxwell-Stefan) or adding a physical term, like adding viscous flow and the pressure diffusion term in the Dusty Gas Model. Please note that the first two terms of the density-based Dusty Gas Model, equation (B.2), produce a singular matrix similar to the above condition, but terms with gradient of pressure regularize the non-singular matrix perfectly. The only option to regularize the density-based formulation of Maxwell-Stefan is to add a physical term to equations, like a convective flux. For a fluid medium it is not possible to generalize a relation between pressure gradient and the mass-averaged velocity as the hydrodynamics is so complex that it can only be obtained from a flow solver. However, for a porous media or a porous-fluid interface, the mass-averaged velocity can be related to the pressure gradient with

$$\vec{V} = -\frac{B_0}{\mu} \nabla p, \tag{51}$$

where B_0 and μ are a geometric factor of a porous material and the viscosity, respectively. This approach is similar to the derivation of the Dusty Gas Model. B_0 is $r^2/8$ for a long, straight, circular capillary of radius r, or $h^2/3$ for a narrow channel with $2h$ width which results to a Poiseuille's flow with equation (51).

Now, the density-based form of the Maxwell-Stefan equations can be regularized for a porous material or at a porous-fluid interface as

$$\begin{aligned} -\rho_i \frac{B_0}{\mu} \nabla p - \sum_j \Gamma''_{ij} \nabla \rho_j &= -\rho_i \frac{B_0}{\mu} R_u T \sum_j \frac{\nabla \rho_j}{M_j} - \sum_j \Gamma''_{ij} \nabla \rho_j \\ &= -\sum_j \tilde{\Gamma}_{ij} \nabla \rho_j, \end{aligned} \tag{52}$$

with

$$\tilde{\Gamma}_{ij} = \Gamma''_{ij} + \frac{\rho_i B_0 R_u T}{\mu M_j}. \tag{53}$$

As mentioned it is not possible to find a suitable B_0 for a general fluid flow scenario because of its complexity. Even for a normal channel or pipe, B_0 will be very big (using a proper dimension to calculate equation (51)) in comparison with components of the matrix $\mathbf{\Gamma''}$, which produces instability in the global matrix solver (in these cases, instead of a flow solver, only the species continuity equations are solved with the total flux formulation, equation (52)). In conclusion, the density-based formulation of the Maxwell-Stefan equations can be used only for a porous media or at a porous-fluid interface.

With the described difficulty with the density-based formulation of the Maxwell-Stefan model, it was decided to adopt two primary variables for the species continuity equations when coupled mass transfer between solid and a fluid is considered. For the fluid part, mass fraction is the primary variable as discussed in section 2, and for the porous media part, species mass density is the primary variable of our system as explained in section 3. At the interface of fluid and solid where the continuity of flux is imposed (48), the equations are written in mass density-based form with the proper regularization of the fluid flux part. Therefore, at each intersect, when the continuity of mass flux is solved, new set of species mass densities at surface is obtained and used as the Dirichlet immersed boundary values explained in section 4.1 to solve a system of equations with mass fraction and species density as primary variables for fluid and solid parts, respectively.

Now the continuity of mass flux at the fluid-solid interface, equation (48), can be written as

$$-\sum_j \tilde{\Gamma}_{b_{ij}} \frac{\partial \rho_j}{\partial n}\Big|_{b_f} = -\sum_j \tilde{\Gamma}'_{b_{ij}} \frac{\partial \rho_j}{\partial n}\Big|_{b_s}. \tag{54}$$

As mentioned above, the normal velocity V_{b_n} is very small, and usually it is negligible, but it can help to regularize the system properly.

In order to calculate the normal gradients in equation (54), numerical probes are used. Fig. 5 depicts an example of probes for an solid-fluid intersect. ϕ_1 and ϕ_2 are probes in the fluid part, and ϕ_{-1} and ϕ_{-2} are probe points in the porous part. Δn is designated as the probe length, the distance between two neighboring probe points. Values of ϕ_1, ϕ_2, ϕ_{-1} and ϕ_{-2} can be written based on the Taylor-series expansion, subsequently the normal gradient of a variable in the fluid or the solid can be obtained. Therefore, the continuity of mass flux can be rewritten as

$$\begin{aligned} &-\sum_j \tilde{\Gamma}_{b_{ij}} \frac{1}{2\Delta n} \left(-3\rho_{b_j} + 4\rho_{1_j} - \rho_{2_j} \right) + \mathcal{O}\left(\Delta n^2\right) \\ &= -\sum_j \tilde{\Gamma}'_{b_{ij}} \frac{1}{2\Delta n} \left(\rho_{-2_j} - 4\rho_{-1_j} + 3\rho_{b_j} \right) + \mathcal{O}\left(\Delta n^2\right). \end{aligned} \tag{55}$$

Probe values both in a fluid medium and a porous material are obtained based on the trilinear interpolation of surrounding cells (in 2D cases, the bilinear interpolation). It should be noted that for the fluid part, in order to obtain ρ_1 and ρ_2 set, not only mass fractions but also pressure and temperature (in case of not isothermal processes) are interpolated at the locations of probes 1 and 2. Then, the species densities are calculated as

$$\rho_i = \frac{p}{R_u T \sum_j \frac{\omega_j}{M_j}} \omega_i. \tag{56}$$

The goal is to update a new set of surface species densities, ρ_b, at each intersect of fluid-solid. Therefore, equation (55) is converted to the following matrix system

$$\mathbf{A}\boldsymbol{\rho}_b = \mathbf{b}, \tag{57}$$

with

$$A_{ij} = 3\left(\tilde{\Gamma}_{b_{ij}} + \tilde{\Gamma}'_{b_{ij}}\right), \tag{58}$$

and

$$b_i = \sum_j \left(\tilde{\Gamma}_{b_{ij}} a_{f_j} - \tilde{\Gamma}'_{b_{ij}} a_{s_j}\right). \tag{59}$$

a_f and a_s vectors in (59) are

$$\begin{aligned} a_{f_i} &= 4\rho_{1_j} - \rho_{2_j}, \\ a_{s_i} &= \rho_{-2_j} - 4\rho_{-1_j}. \end{aligned} \tag{60}$$

After the system of equations in equation (57) is solved at each intersect of fluid-solid, a new set of species densities and mass fractions, equation (61), are used as the immersed boundary values for the inside and the outside of a particle, respectively.

$$\omega_{b_i} = \frac{\rho_{b_i}}{\sum_j \rho_{b_j}}. \tag{61}$$

In addition, the normal velocity at each intersect is calculated as

$$V_{b_n} = -\frac{B_0}{\mu}\frac{1}{2\Delta n} R_u T \sum_j \frac{-3\rho_{b_j} + 4\rho_{1_j} - \rho_{2_j}}{M_j}. \tag{62}$$

Then, based on the unit normal vector at intersect ($\hat{n}$), it is decomposed to $\left[V_{b_n}\hat{n}_x, V_{b_n}\hat{n}_y, V_{b_n}\hat{n}_z\right]^T$ and used as the immersed boundary values for the velocity field in the flow solver. If for some cells of the staggered (momentum) grid, there is no direct intersect at the immersed boundary (Fig. 6), interpolation is used to calculate the Dirichlet velocity at that point based on other available velocity values at the interface. It should be noted that the Maxwell-Stefan diffusion matrix ($\mathbf{\Gamma}$) and the total flux of the Dusty Gas Model ($\tilde{\mathbf{\Gamma}}'$) at each intersect of the fluid-solid are calculated and updated as well by the newly obtained species densities at the same point.

Furthermore, not only is the bulk density field as usual updated after the mass transport part (please look at point 3 in section A), but also the velocity field for faces (velocities are stored at faces of control volume cells in our in-house code) which are located inside a particle is updated by

$$\vec{V}_s = -\frac{\sum_i \sum_j \tilde{\Gamma}'_{ij} \nabla \rho_{s_j}}{\sum_j \rho_{s_j}}. \tag{63}$$

Both the nominator and denominator of equation (63) should be evaluated at the face where a corresponding velocity component needs to be updated. Subscript "s" refers to a solid medium. For calculation of $\nabla\rho_s$ at the nominator, central differencing is used with the values of species densities from both sides of a cell, if both center of neighbor cells are located in the solid part, Fig. 7. Otherwise, the following relation is used to calculated the gradient of species densities, Fig. 8,

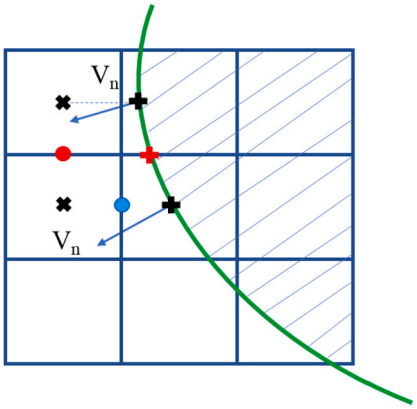

Fig. 6. The red circle points to the center of a staggered grid for the y-momentum equation. This fluid cell has a solid neighbor at East. Here, the y-component of velocity should be known at the red cross point at the immersed boundary. As there is not direct intersect of scalar field available at the red cross point, velocity should be interpolated based on values at the two black cross points in the neighbor.

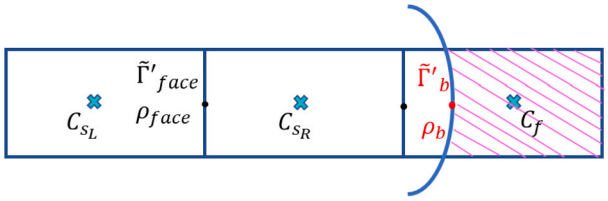

Fig. 7. Velocity is interpolated at "face" which is located inside the solid particle. C_{s_L} and C_{s_R} represent centers of two solid faces that have a shared face. $\tilde{\mathbf{\Gamma}}'_b$ and ρ_b are the total flux matrix of the Dusty Gas Model and the species densities at the fluid-solid intersect, respectively.

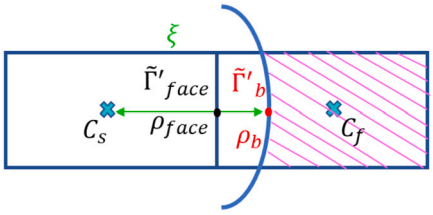

Fig. 8. Velocity is interpolated at "face" that is located inside the solid particle. C_s and C_f represent centers of the solid and the fluid cells. ξ is used for the matrix coefficient manipulation of the fluid cell with center at C_f. $\tilde{\mathbf{\Gamma}}'_b$ and ρ_b are the total flux matrix of the Dusty Gas Model and species densities at the fluid-solid intersect, respectively.

$$\left.\frac{\partial \rho_{s_j}}{\partial x}\right|_{face} = \frac{\rho_{b_j} - \rho_{C_s}}{\xi}. \tag{64}$$

In other directions, the same approach is used.

ρ_s and the Dusty Gas Model total flux matrix ($\tilde{\mathbf{\Gamma}}'$) should be interpolated at each face. If the center of both neighboring cells are in a solid medium, then the value at face is interpolated as an average of the central values of both neighbors, Fig. 7. In cases where one of the center of neighbor cells is located in a fluid medium, Fig. 8, interpolation of the Dusty Gas Model total flux matrix and species densities are based on the following weighted relations

$$\tilde{\mathbf{\Gamma}}'_{face} = \frac{0.5}{\xi}\tilde{\mathbf{\Gamma}}'_b + \frac{\xi - 0.5}{\xi}\tilde{\mathbf{\Gamma}}'_{C_s}, \tag{65}$$

and

$$\rho_{s_{b_{face_j}}} = \frac{0.5}{\xi}\rho_{b_j} + \frac{\xi - 0.5}{\xi}\rho_{C_{s_j}}. \tag{66}$$

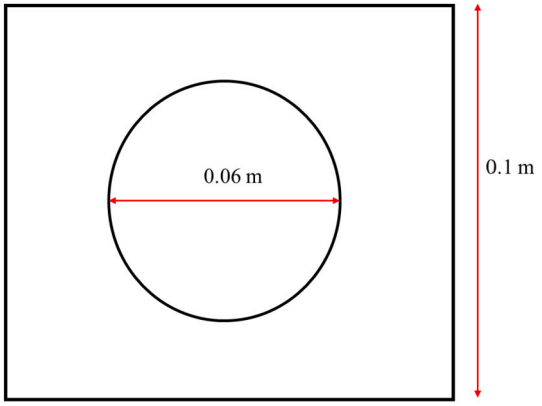

Fig. 9. Coupled mass transfer test case's geometry. A porous particle is located in the middle of a box.

4.3. Verification test cases

Fig. 9 depicts the test case that is designed to assess the performance of the developed coupled mass flux formulation in this study. A porous particle is located in the center of a box. A ternary mixture is chosen as the fluid medium. The geometrical properties of the porous material are the same as described in section 3.2.2. At the initial condition, two different sets of mass fractions are used for interior and exterior of the particle (the mass fraction set for the inside is converted to the species density set, as we have two primary variables in our model). Pressure and temperature are uniform $p = 200000$ Pa and $T = 300$ K at the initial condition. At steady state, a spatially uniform composition is reached for the entire domain. The wall boundary condition is imposed for all faces of the box with the Neumann boundary condition for species. At the immersed boundary the continuity of flux is imposed. The grid resolution is 100×100 in all test cases. Time step is set to 1×10^{-2} s in all test cases reported below. Smaller time steps do not produce more accurate results in the presented test cases. B_0 is calculated as $\frac{r_p^2}{8.0}$, with r_p as the pore radius, when the normal velocity is required for the regularization of the continuity of mass flux formulation at each intersect of fluid-solid, equations (53) and (62).

4.3.1. First set

In this test case, N_2, Ar, and He are chosen as the mixture. The following set of mass fractions are used to initialize inside and outside of the particle

- Fluid part initial mass fractions $\{0.314941, 0.0, 0.685059\}$,
- Solid porous part initial mass fractions $\{0.0, 0.3, 0.7\}$.

For the binary diffusion coefficients, the same set presented in Table 5 is used here as well.

Table 7 compares the obtained results with and without regularization for the mass flux continuity formulation with the analytical solution at the steady-state condition. Note that the velocity at the immersed boundary is set to zero (no regularization) for the results without regularization. Basically, the Maxwell-Stefan equations are converted to the species density form, but no regularization by the convective term (explained in equation (53)) is imposed to resolve the singularity in the fluid part of the mass flux continuity.

As is clear both models are able to replicate the analytical solution. However, the unregularized model requires 19 times more iterations to reach the steady-state condition.

Fig. 10 presents the time evolution of the mass flux at a immersed boundary point for the three species in this test case. The immersed boundary point at the particle surface has a 45.78° angle with respect to the horizontal line that passes the center of the particle. As evident from the figure, the mass fluxes are non-zero at the beginning due to the difference in inside and outside mass fractions, then they merge to zero as the equilibrium condition is obtained. Fig. 11 shows the mass fraction profiles along a horizontal line passing through the center of the particle, evolving in time toward the equilibrium.

Table 7
The comparison of the numerical versus the analytical solution for the coupled mass transfer test case described in section 4.3.1.

	Analytical	Regularized Model	Unregularized Model
ω_{N_2}	0.225876	0.226525	0.224894
ω_{Ar}	0.08484	0.0842244	0.085734
ω_{He}	0.689284	0.689251	0.689372
Total Mass [gr]	4.39602	4.39602	4.39602

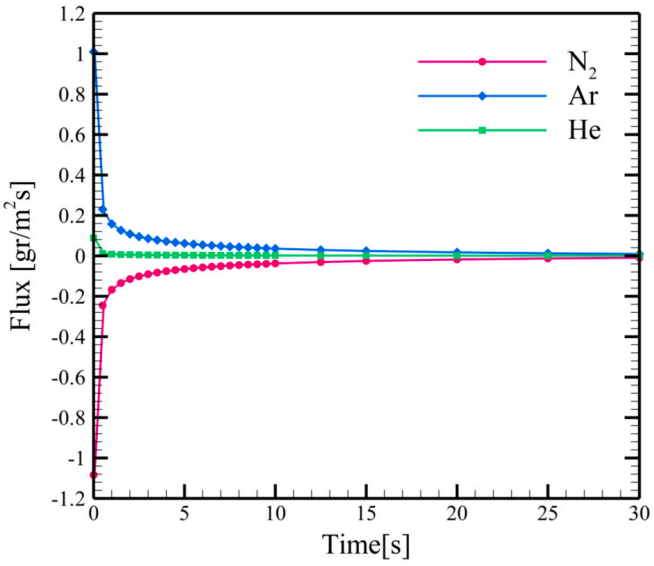

Fig. 10. The variation of the mass flux for N_2, Ar, and He at a solid-fluid boundary versus time for the test case presented in section 4.3.1. The point at the particle boundary has a 45.78° angle with respect to the horizontal line that passes the center of the circle.

Table 8
The used binary diffusion coefficients for the described test case in section 4.3.2.

Species pair	Binary Diffusion Coefficient [m^2/s]
N_2-Ar	1.95×10^{-5}
N_2-H_2O	2.747×10^{-5}
Ar-H_2O	2.5×10^{-5}

4.3.2. Second set

In this test case, N_2, Ar, and H_2O are chosen as the mixture. Bigger differences between the inside and outside compositions of the particle are imposed in comparison to the previous test case. The following set of mass fractions are used to initialize inside and outside of the particle

- Fluid part initial mass fractions $\{0.030813, 0.5, 0.469187\}$,
- Solid porous part initial mass fractions $\{0.8, 0.0, 0.2\}$.

The binary diffusion coefficients that are used in this test case are presented in Table 8.

Table 9 compares the obtained results at the steady state condition between numerical models and the analytical solution. The model that

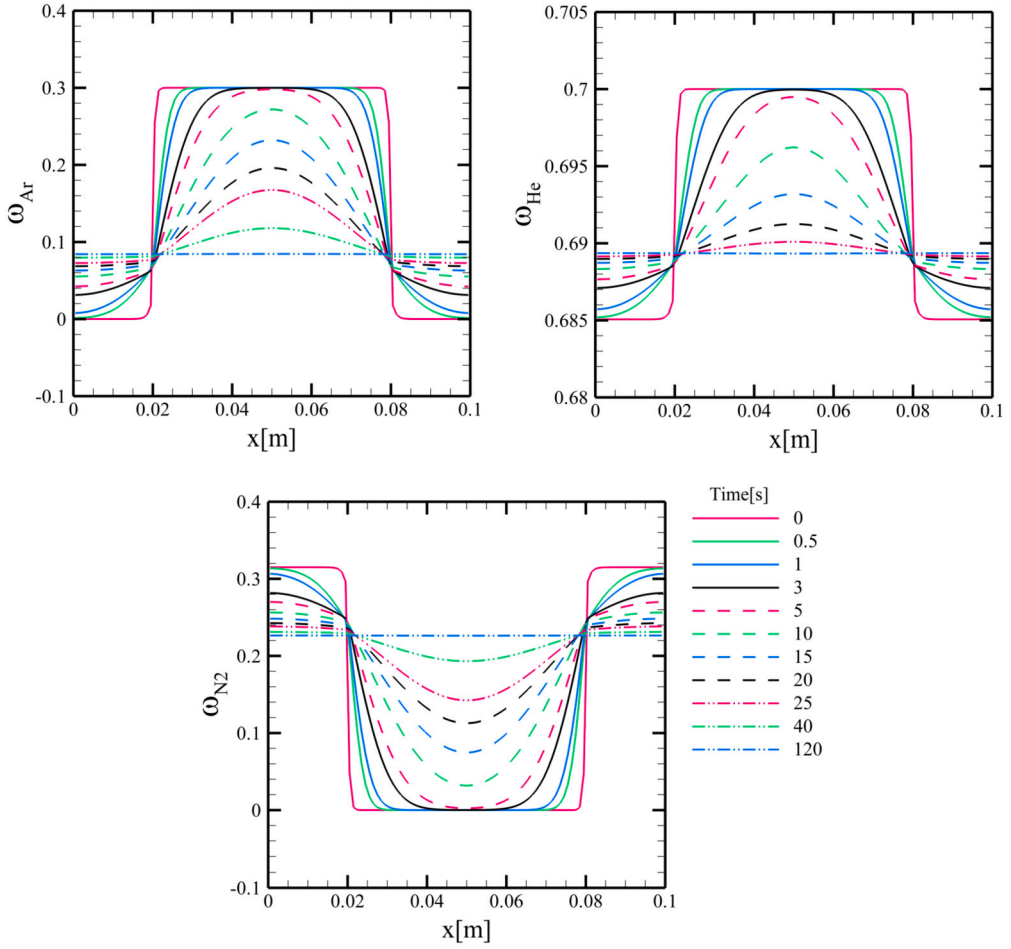

Fig. 11. The variations of mass fractions for Ar, He, and N_2 versus time along the horizontal line that passes the center of the particle for the coupled mass transfer test case presented in section 4.3.1.

Table 9
The comparison of the numerical versus the analytical solution for the coupled mass transfer test case described in section 4.3.2.

	Analytical	Regularized Model	Unregularized Model
ω_{N_2}	0.248339	0.241846	nonphysical
ω_{Ar}	0.3586	0.362384	nonphysical
ω_{H_2O}	0.393061	0.395769	nonphysical
Total Mass [gr]	20.2177	20.2177	nonphysical

uses the normal component of velocity V_{b_n} at the immersed boundary for the regularization of the fluid part of the mass flux continuity relation, equation (48), can obtain accurate results. However, the model that sets $V_{b_n} = 0$ is not able to produce physical results due to the fact that the density form of Maxwell-Stefan equations is singular. Nonphysical results are obtained with average values for mass fractions around $\{0.8374, 0.05867, 0.12017\}$ which violated the conservation of mass $\sum_j \omega_j = 1.016$. In addition, equilibrium is not obtained in the entire simulation domain for the unregularized model.

Fig. 12 shows the variation of the mass flux for the involved species in this test case versus time for a point that has a 45.78° angle with respect to the horizontal line that passes through the center of the particle. As expected the fluxes converge to zero as the simulation approaches to the steady-state condition. In addition, Fig. 13 depicts the mass fraction variation of all three species in this test case over the horizontal line that passes the center of the particle for different times of the simula-

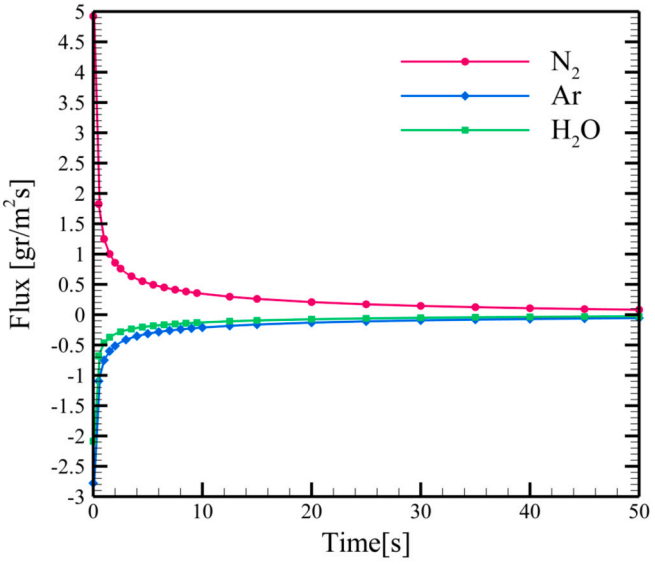

Fig. 12. The variation of the mass flux for N_2, Ar, and H_2O at a solid-fluid boundary point versus time for the test case presented in section 4.3.2. The point at the particle boundary has a 45.78° angle with respect to the horizontal line that passes the center of the circle. The results are obtained with the regularized model.

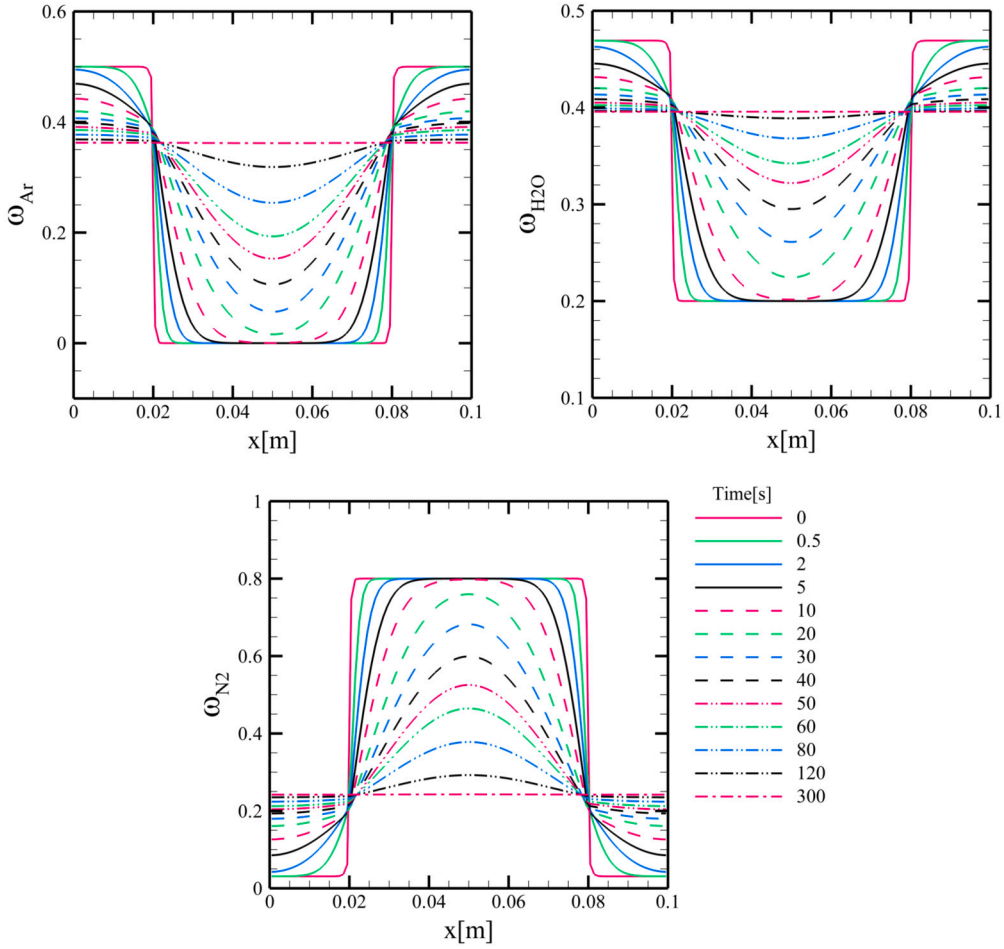

Fig. 13. The variations of mass fractions for Ar, H_2O, and N_2 versus time along the horizontal line that passes through the center of the particle for the coupled mass transfer test case presented in section 4.3.2. The results are obtained with regularized model.

Table 10
The comparison of the numerical versus the analytical solution for the coupled mass transfer test case described in section 4.3.3.

	Analytical	Regularized Model	Unregularized Model
ω_{N_2}	0.660721	0.654883	Nan
ω_{Ar}	0.15554	0.158909	Nan
ω_{H_2O}	0.183739	0.186209	Nan
Total Mass [gr]	21.2807	21.2807	Nan

tion. Note that both figures are for the model with regularization where V_{b_n} is used to regularized the singular density base Maxwell-Stefan flux matrix at the immersed boundary.

4.3.3. Third set

In this test case N_2, Ar, and H_2O are chosen as the mixture. The compositions of interior and exterior of the particle possess the highest gradients in comparison with the last two test cases. The following set of mass fractions are used to initialize inside and outside of the particle

- Fluid part initial mass fraction $\{0.9, 0.0, 0.1\}$,
- Solid porous part initial mass fraction $\{0.053894, 0.55, 0.396106\}$.

Table 10 compares again the obtained results obtained from the numerical simulations with the analytical solution. Similar to the other two cases, one model uses V_{b_n} at the immersed boundary as a physical term to regularize the singular density base Maxwell-Stefan diffusive

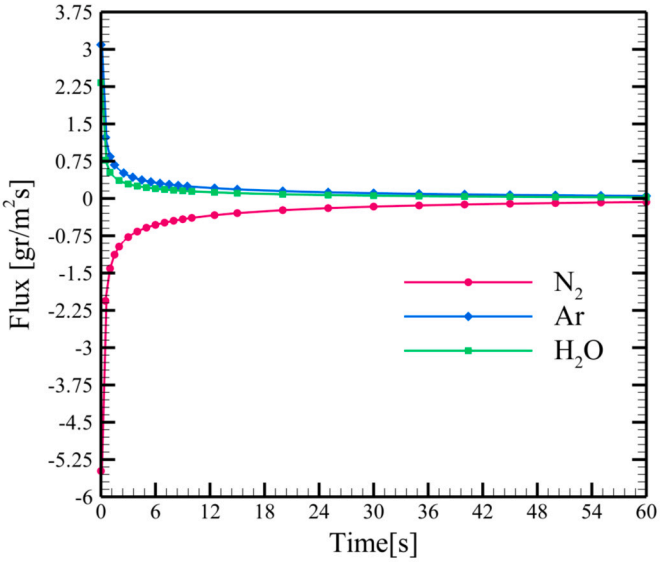

Fig. 14. The variation of the mass flux for N_2, Ar, and H_2O at a solid-fluid boundary point versus time for the test case presented in section 4.3.3. The point at the particle boundary has a 45.78° angle with respect to the horizontal line that passes the center of the circle. The results are obtained with the regularized model.

flux, and the other sets $V_{b_n} = 0$ and keeps the fluid part of the continuity of mass flux, equation (48), singular. As evident from the results

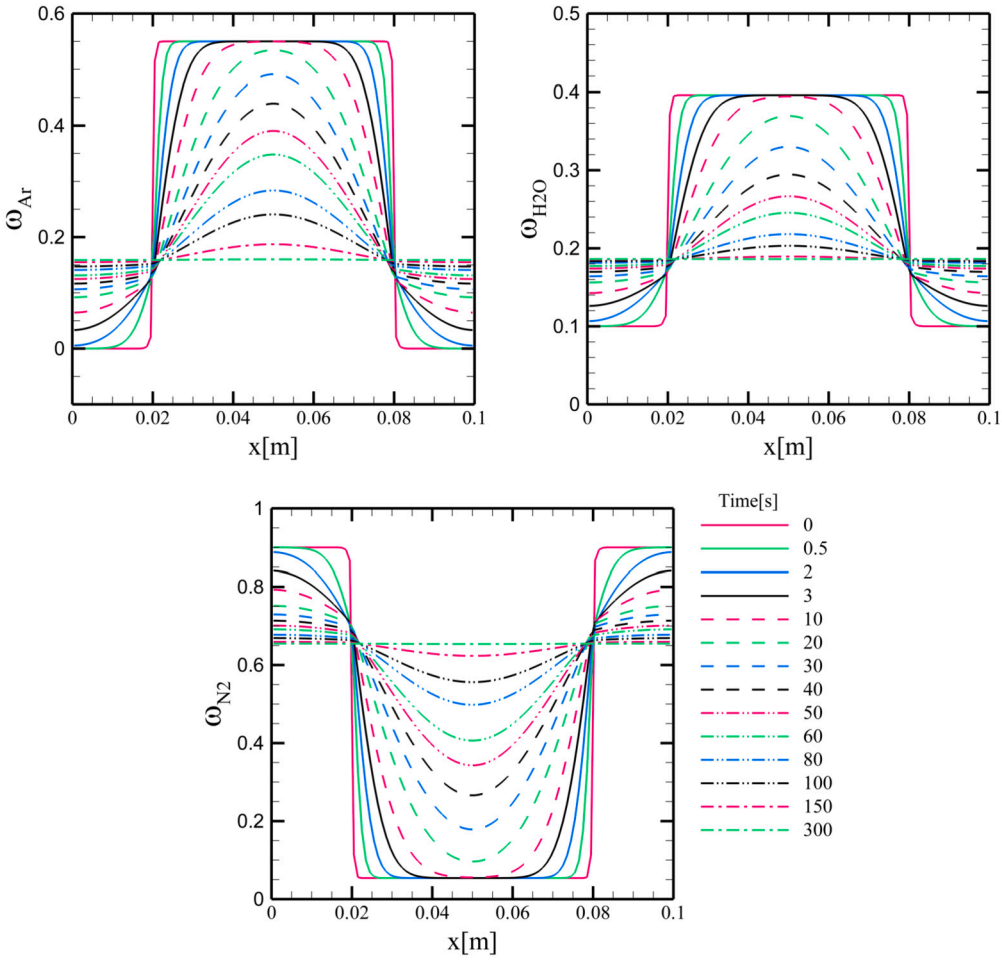

Fig. 15. The variations of mass fractions for Ar, H_2O, and N_2 versus time along the horizontal line that passes through the center of the particle for the coupled mass transfer test case presented in section 4.3.3. The results are obtained with the regularized model.

presented in Table 10, only the model with physical regularization is able to produce meaningful results in this test case. For the model with $V_{b_n} = 0$ and the singular diffusive flux of the Maxwell-Stefan equations even nonphysical values like the previous test Case 4.3.2 are not obtained. The model diverges after a couple of iterations.

Figs. 14 and 15 present the variation of the species mass fluxes and mass fractions over time for the regularized model, respectively. As is expected, fluxes vanish at the immersed boundary as the model marches in time and the equilibrium condition is obtained. The gradients in the mass fractions interior and exterior to the particle decreases over time until constant values (equilibrium condition) are attained in the entire simulation domain.

4.4. Spatially variable test case

In this case, the geometrical and physical parameters are the same as Fig. 9 and the previous test case, section 4.3.3. The only difference is the boundary conditions at the east and west edges of the numerical domain. Here, the Dirichlet boundary conditions are set with two different sets of mass fractions for the east and the west faces $\{N_2, Ar, H_2O\}$.

- The west face Dirichlet boundary conditions for mass fractions $\{0.9, 0.0, 0.1\}$,
- The east face Dirichlet boundary conditions for mass fractions $\{0.053894, 0.55, 0.396106\}$.

Fig. 16 shows the spatially variation of mass fractions at the steady state condition in the numerical domain. In addition Fig. 17 depicts the variation of mass fractions along the horizontal line that passes the center of the particle. As is clear, the slope of variations of mass fractions is different interior and exterior to the particle due to different physical conditions. Furthermore, the presented results in Fig. 16 prove that the methodology works well and satisfies mass conservation for the spatially inhomogeneous situations.

4.5. Active flow test case

For this test case a particle in a flow is considered, where the inlet velocity corresponds to Re = 10, based on the particle diameter. The geometry of the numerical domain is changed compared to the Fig. 9. The new domain has a width 0.2 m and a length of 0.8 m. The porous particle has the same radius as in the previous test cases, 0.03 m. The center of the particle is located at (0.1 m, 0.1 m). The velocity and composition are fixed at the west edge of the domain (the inlet). The inlet mass fractions for the mixture $\{N_2, Ar, H_2O\}$ are set to $\{0.9, 0.0, 0.1\}$. At the outlet, the pressure is set to 200000 Pa. The viscosity and binary diffusion coefficients are the same as in the previous test cases. The initial mass fractions for the porous particle are $\{0.053894, 0.55, 0.396106\}$. The numerical domain is elongated to form a fully developed velocity at the outlet. The used grid resolution is 200×800 grid for this test case.

Figs. 18 and 19 show the velocity contours for the horizontal and vertical component of the velocity at the steady state condition, respec-

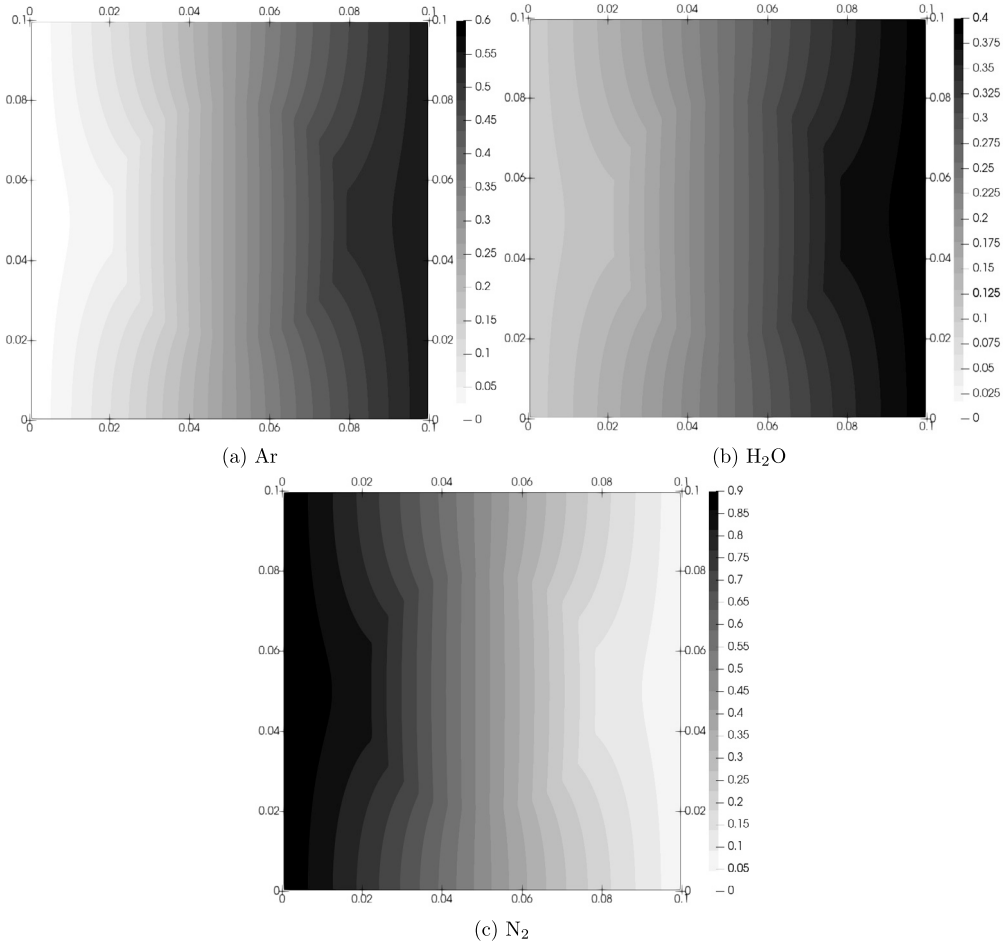

Fig. 16. The variations of mass fractions for Ar, H_2O, and N_2 in the numerical domain for the coupled mass transfer test case presented in section 4.4. The results are obtained with the regularized model.

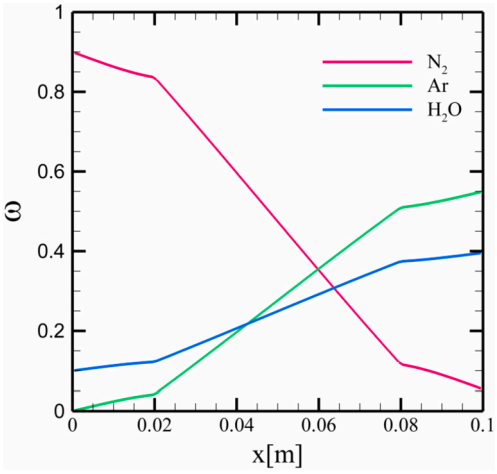

Fig. 17. The variation of the mass fractions of N_2, Ar, and H_2O over the line that passes the center of the particle at the steady state condition for the test case presented in section 4.4. The results are obtained with the regularized model.

tively. In addition, Figs. 20 and 21 show the variations of the mass fractions versus time for all species over the line that passes the center of the particle. As it is expected, the inlet composition washes away the composition inside the porous particle, and the uniform composition is obtained at the steady state.

This test case shows a proof of concept for the conditions that convection plays role. More complex geometries, more particles, higher Reynolds numbers and reactions are all scenarios that are out of the scope of this paper and are outlined as future research extended on top of the presented symmetric methodology.

5. Conclusion

A detailed description of the newly developed numerical methodology to capture the multicomponent mixture physics in fluid-solid media is presented in this study. In this methodology all components of a mixture are numerically treated similar, so the methodology is symmetric. There is no need to select one species in advance to impose the relevant mass and flux conservation constraints on the governing system of equations. Then, the symmetric approach paves the way to more accurate simulations of complex processes like Fisher-Tropch in chemical reactors.

In the presented methodology, the Maxwell-Stefan equations are coupled with a compressible flow solver to model the convection and the diffusion of the fluid medium. A symmetric and conservative formulation of the Maxwell-Stefan equations from Peerenboom et al. (2011) study is chosen for the implementation in this work. It is found that only the formulation based on the diffusive flux is numerically stable. In addition, the correct regularization of the diffusive flux matrix for this specific form is presented in this paper.

The Maxwell-Stefan equations are extended into the porous media with the help of the Dusty Gas Model. A robust and self-consistent for-

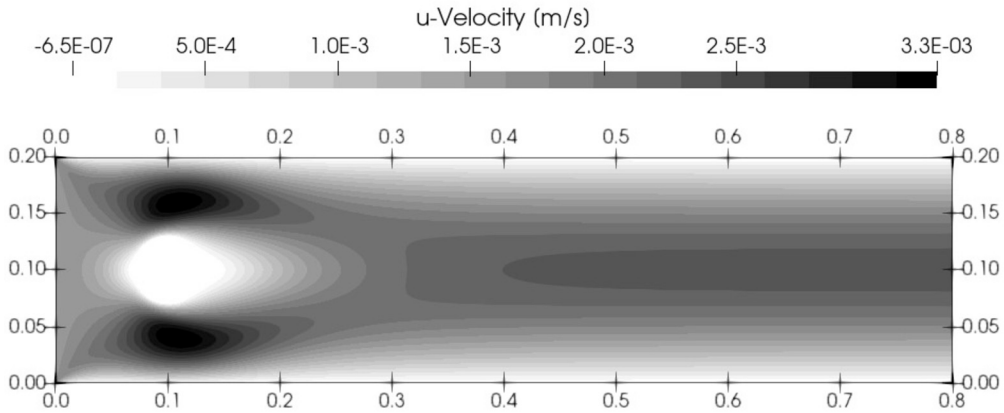

Fig. 18. The contour of the horizontal component of velocity (u) at the steady state condition for the test case presented in section 4.5. The Reynolds number at the inlet is set to 10. The results are obtained with the regularized model.

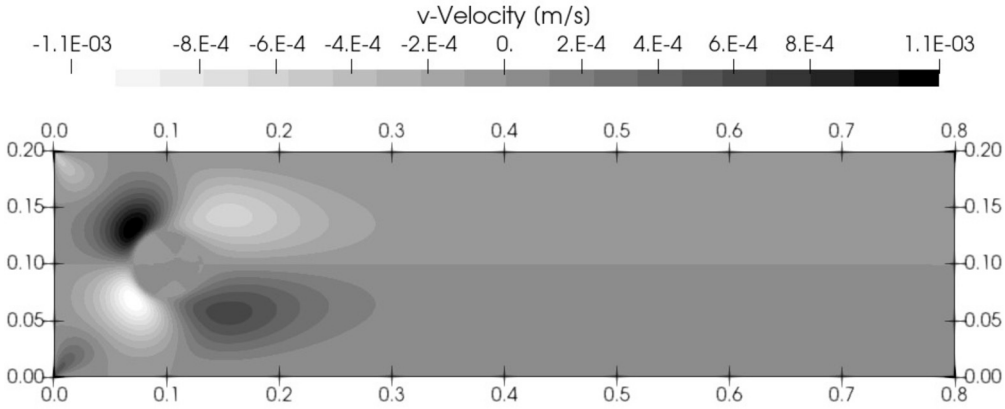

Fig. 19. The contour of the vertical component of velocity (v) at the steady state condition for the test case presented in section 4.5. The Reynolds number at the inlet is set to 10. The results are obtained with the regularized model.

mulation of the Dusty Gas Model is developed. It is shown that the formulation is unconditionally stable under any circumstances, with or without a gradient of pressure over a porous medium. In this formulation, all transport phenomena (different diffusion mechanisms and viscous flow) are coupled directly by rewriting all the terms in the DGM based on species mass densities.

Finally, the ghost-cell Immersed Boundary Method is used to couple the fluxes in the fluid and the solid phases on the particle's boundary. In order to capture the coupled mass transfer, continuity of mass flux is imposed in the normal direction for each fluid-solid intersect. The developed methodology is based on two primary variables for a multi-component system. Mass fraction for the fluid part where the Maxwell-Stefan equations are coupled with the compressible flow solver, and species density for the porous material part where the Dusty Gas Model captures the physics. A novel formulation of the continuity of mass flux has been developed where the surface normal velocity is used for regularization of the density-based Maxwell-Stefan equations of the fluid part. It has been shown and proven that the regularization not only decreases computational expenses of a model but also is necessary to produce physical results and to avoid divergence. In addition, several test cases are designed for verification of the developed methodology. These newly established test cases can be used as benchmarks for the validation of future research.

Applying the developed methodology for a reactive mixture with the non-isothermal condition and multiple particles can further assess the performance and robustness of the methodology in conditions which are close to packed bed reactors.

CRediT authorship contribution statement

S. Tadayon Mousavi: Writing – original draft, Writing – review & editing, Methodology, Software, Validation, Formal analysis, Conceptualization. **C.M.Y. Claassen:** Writing – review & editing, Software. **M.W. Baltussen:** Writing – review & editing, Supervision, Funding acquisition. **E.A.J.F. Peters:** Writing – review & editing, Supervision, Formal analysis, Conceptualization, Funding acquisition. **J.A.M. Kuipers:** Writing – review & editing, Supervision, Funding acquisition.

Declaration of competing interest

The authors declare that they have no known competing financial interests or personal relationships that could have appeared to influence the work reported in this paper.

Data availability

Data will be made available on request.

Acknowledgement

This work was supported by the Netherlands Center for Multiscale Catalytic Energy Conversion (MCEC), and NWO Gravitation programme funded by the Ministry of Education, Culture and Science of the government of the Netherlands. Grant number: MCEC.2-TUE-2-15.

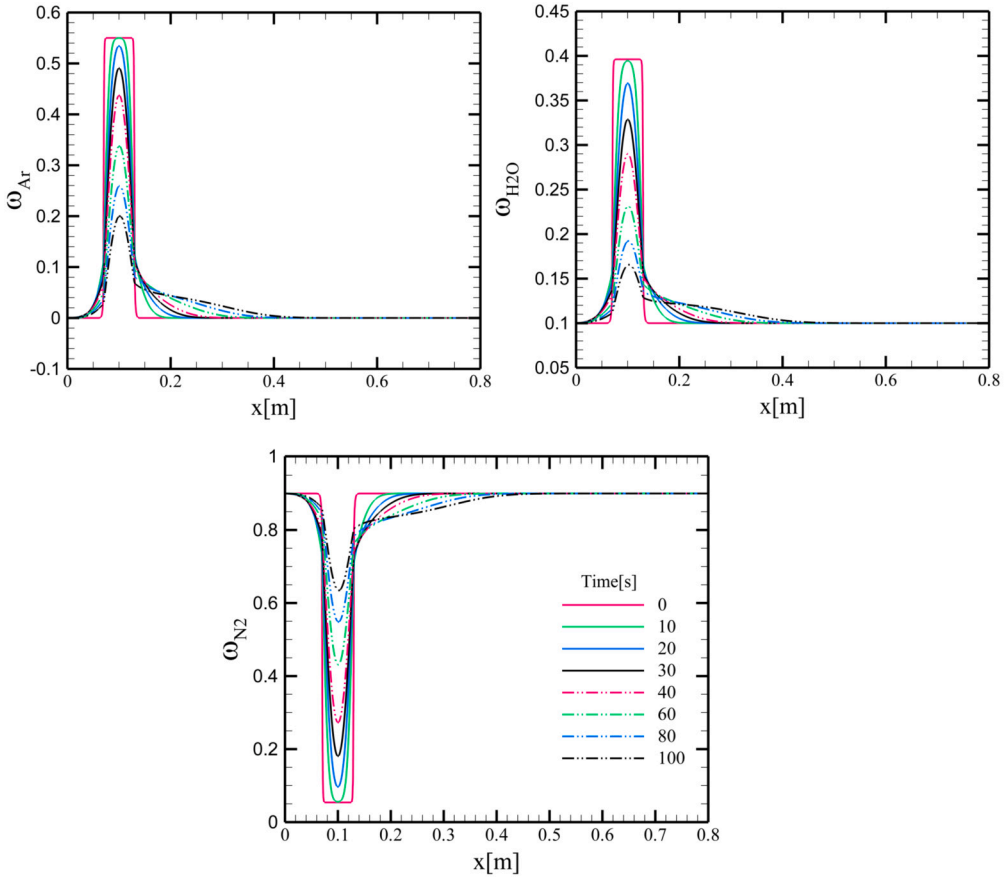

Fig. 20. The variations of mass fractions for Ar, H_2O, and N_2 versus time for the first 100 s of simulation along the horizontal line that passes through the center of the particle for the conjugate mass transfer test case presented in section 4.5 where the inlet velocity is set for Re = 10. The results are obtained with the regularized model.

Appendix A. The pressure correction algorithm

For each time step, the following steps are taken for coupling the compressible flow solver with the mass transfer equations:

1. Solve the bulk momentum equations (27) based on a guessed pressure and density fields. For the first time step, employ the initial condition pressure and density fields. In subsequent time steps, use the pressure field from the previous time step along with the updated density field obtained from equation (A.2) at the end of the preceding time step.
2. Calculate the mass defect for each cell with the updated velocity field $\vec{V}^{n+1}$ (from step 1 for the first iteration of a current time step of the flow solver and from step 6 for the other iterations) by using the discretized form of the conservative form of the continuity equation (29)

$$\mathbb{D}_{i,j,k} = \frac{\mathcal{V}}{\Delta t}\left[\rho^{n+1}_{i,j,k} - \rho^{n}_{i,j,k}\right] + \left[(A\rho u)^{n+1}_{i+1/2,j,k} - (A\rho u)^{n+1}_{i-1/2,j,k}\right] + \left[(A\rho v)^{n+1}_{i,j+1/2,k} - (A\rho v)^{n+1}_{i,j+1/2,k}\right] + \left[(A\rho v)^{n+1}_{i,j,k+1/2} - (A\rho v)^{n+1}_{i,j,k+1/2}\right], \quad \text{(A.1)}$$

with $\vec{V} = [u, v, w]^T$, $\mathcal{V}$ and A stand for the volume and the face area of a cell. Δt represents the time step. Note that ρ^n is either from the initial condition bulk density field for the first time step of a model, or from the density field at the end of the flow solver part of the previous time step for the other time steps. ρ^{n+1} is

- from the initial condition of the density field when the algorithm is in the first time step and the first iteration of the flow solver,
- from step 5 when it is not the first iteration of the flow solver,
- from the end of the previous time step (when the bulk density field is updated after updating mass fraction fields) when it is the first iteration of a time step (when current time of a model is not zero).

3. Check whether the maximum mass defect in the domain is lower than the defined threshold, or the current iteration count exceeds the maximum number of iterations for each time step of the flow solver.
   - If yes, the momentum equation (flow solver) part is finished. Subsequently the species continuity equations are solved based on the updated pressure, the velocity, and the bulk density fields. After mass fractions fields are updated (unknowns of the species continuity equations)

     First Store the current density field as "old" (ρ^n),

     Second Update the density field with the new mass fractions based on the ideal gas law

     $$\rho = \frac{p}{R_u T \sum_i \frac{\omega_i}{M_i}}, \quad \text{(A.2)}$$

     with R_u as the universal gas constant (Kuo, 2005). Note that the used pressure field in equation (A.2) is the updated field at the end of the flow solver part,

     Third Go to the next time step (step 1).

   - If no, go to step 4.

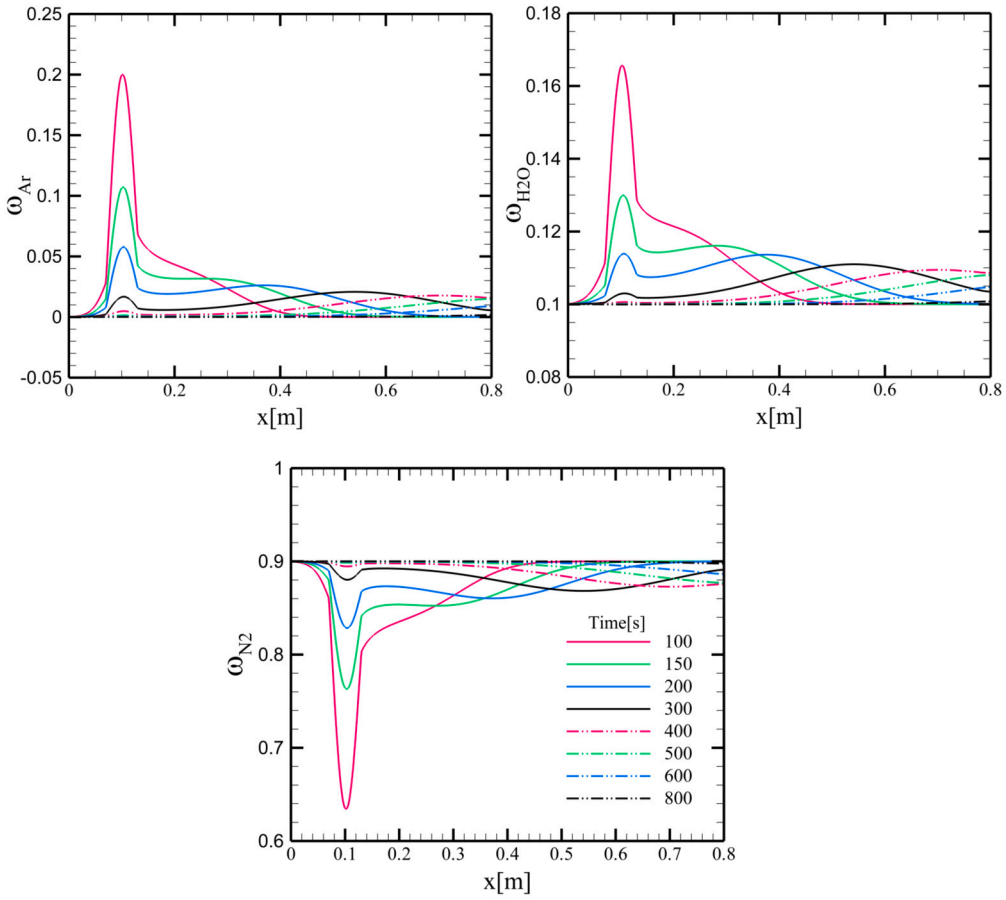

Fig. 21. The variations of mass fractions for Ar, H_2O, and N_2 versus time for 100 to 800 s of simulation along the horizontal line that passes through the center of the particle for the conjugate mass transfer test case presented in section 4.5 where the inlet velocity is set for Re = 10. The results are obtained with the regularized model.

4. Update the pressure field with the pressure correction p' by solving the following equation over the entire numerical domain

$$\mathbf{J_p p'} = -\mathbf{D}, \tag{A.3}$$

with $J_{p_{i'j'}} = \frac{\partial \mathbb{D}_{i'}}{\partial p_{j'}}$ represents the whole-field Jacobian. i' and j' define the indices of the component that lays in row i' and column j' of the Jacobian. These indices are calculated based on a proper map between the numerical domain (grid indices) and the chosen data structure for the matrix solver in our in-house code. Component $J_{i'j'}$ of the Jacobian matrix presents the derivative of the mass defect of cell (i, j, k) (A.1) whose indices are mapped into i' with respect to the pressure at the center of a cell whose indices are mapped into j'. The Jacobian is calculated from the terms that are considered new $(n+1)$ in the defect equation (A.1). For instance, if i' represents the cell (i, j, k) and j' represents the pressure $p_{i,j,k}$, then we have

$$J_{p_{i'j'}} = \frac{\partial \mathbb{D}_{i,j,k}}{\partial p_{i,j,k}} = \frac{\forall}{\Delta t R_u T_{i,j,k} \sum_e \frac{\omega_{i,j,k,e}}{M_e}} + 2\frac{A\Delta t}{\Delta x} + 2\frac{A\Delta t}{\Delta y} + 2\frac{A\Delta t}{\Delta z}. \tag{A.4}$$

The first term in the above relation is calculated from the ideal gas law and due to the contribution of $\rho^{n+1}_{i,j,k}$ in the mass defect equation (A.1). The other terms are calculated by the discretized momentum equations for all 3 components of the velocity over the 6 faces of a control volume. Δx, Δy and Δz represent the cell sizes in the three coordinate directions x, y, z. As an example for the off-diagonal term of the Jacobian matrix, consider the component of the Jacobian matrix where i' represents the cell (i, j, k) and j' represents the pressure $p_{i+1,j,k}$, then the off-diagonal term of the Jacobian matrix has the following form

$$J_{p_{i'j'}} = \frac{\partial \mathbb{D}_{i,j,k}}{\partial p_{i+1,j,k}} = -\frac{A\Delta t}{\Delta x}. \tag{A.5}$$

After the solution (p') of equation (A.3) is calculated, the pressure field is updated $p^{n+1} = p^n + p'$. Basically, the pressure field should be modified in such a way that the mass defect is less than a predefined tolerance.

5. Update the bulk density field with the updated pressure based on the ideal gas law. Note that the mass fractions are used in equation (A.2) are from the last time step (after species continuity equations are solved and mass fractions are updated).
6. Update the velocity field with the pressure correction field (p')

$$u^{n+1}_{i+1/2,j,k} = \frac{1}{\rho^{n+1}_{i+1/2,j,k}} \left[\rho^*_{i+1/2,j,k} u^*_{i+1/2,j,k} - \frac{\Delta t \left(p'_{i+1,j,k} - p'_{i,j,k} \right)}{\Delta x} \right],$$
$$u^{n+1}_{i-1/2,j,k} = \frac{1}{\rho^{n+1}_{i-1/2,j,k}} \left[\rho^*_{i-1/2,j,k} u^*_{i-1/2,j,k} - \frac{\Delta t \left(p'_{i,j,k} - p'_{i-1,j,k} \right)}{\Delta x} \right], \tag{A.6}$$

with u^* present the latest update of velocity field in the current time step. ρ^{n+1} is the updated density field in step 5 interpolated

at a face. $\rho*$ is the density field before the update at the step 5. Equation (A.6) is also used for updating the other components of velocity at different faces.

7. Go to the step 2.

Appendix B. Derivation of the unconditional stable formulation of the Dusty Gas Model

The first term of the Dusty Gas Model flux in equation (39) can be written as

$$-\sum_j \Gamma'_{ij}\nabla\omega_j = -\sum_j \Gamma'_{ij}\nabla\left(\frac{\rho_j}{\rho}\right) = -\sum_j \frac{\Gamma'_{ij}}{\rho}\nabla\rho_j + \sum_j \frac{\Gamma'_{ij}}{\rho^2}\rho_j\nabla\rho. \quad \text{(B.1)}$$

The above equation can be replaced with

$$-\sum_j \Gamma'_{ij}\nabla\omega_j = -\sum_j \frac{\Gamma'_{ij}}{\rho}\nabla\rho_j + \sum_j \frac{\Gamma'_{ij}}{\rho^2}\rho_j \sum_k \nabla\rho_k, \quad \text{(B.2)}$$

as

$$\rho = \sum_i \rho_i. \quad \text{(B.3)}$$

The second term of the Dusty Gas Model flux, equation (39), can be modified as

$$-\sum_j H'^{-1}_{ij} S_j = -\sum_j H'^{-1}_{ij} \frac{\sigma M}{M_j}\frac{\rho_j}{\rho}\frac{R_u T}{p}\sum_k \frac{\nabla\rho_k}{M_k} - \sum_j H'^{-1}_{ij} \frac{\sigma M}{M_j D_{jK}}\frac{\rho_j}{\rho}\frac{B_0}{\mu}R_u T\sum_k \frac{\nabla\rho_k}{M_k}, \quad \text{(B.4)}$$

and with further arrangements as

$$-\sum_j H'^{-1}_{ij} S_j = -\sum_j H'^{-1}_{ij} s_{1_j}\sum_k \frac{\nabla\rho_k}{M_k} - \sum_j H'^{-1}_{ij} s_{2_j}\sum_k \frac{\nabla\rho_k}{M_k}, \quad \text{(B.5)}$$

with

$$s_{1_i} = \frac{\sigma M}{M_i}\frac{\rho_i}{\rho}\frac{R_u T}{p},$$
$$s_{2_i} = \frac{\sigma M}{M_i D_{iK}}\frac{\rho_i}{\rho}\frac{B_0}{\mu}R_u T. \quad \text{(B.6)}$$

Note that, the following form of the ideal gas law is used in the derivation of equation (B.5)

$$p = R_u T\sum_i \frac{\rho_i}{M_i}. \quad \text{(B.7)}$$

Then, the species continuity equation based on the density based Dusty Gas Model is

$$\frac{\partial\rho_i}{\partial t} - \nabla\cdot\left(\sum_j \frac{\Gamma'_{ij}}{\rho}\nabla\rho_j\right) + \nabla\cdot\left(\sum_j \frac{\Gamma'_{ij}}{\rho^2}\rho_j\sum_k \nabla\rho_k\right) - \nabla\cdot\left(\sum_j H'^{-1}_{ij} s_{1_j}\sum_k \frac{\nabla\rho_k}{M_k}\right) - \nabla\cdot\left(\sum_j H'^{-1}_{ij} s_{2_j}\sum_k \frac{\nabla\rho_k}{M_k}\right) = r_i. \quad \text{(B.8)}$$

The compacted format of the above equation (B.8) is presented in the main part of the paper (section 3.1, equation (40)).

References

Bothe, D., Druet, P., 2023. On the structure of continuum thermodynamical diffusion fluxes—a novel closure scheme and its relation to the Maxwell–Stefan and the Fick–Onsager approach. Int. J. Eng. Sci. 184, 103818.

Chandra, V., Peters, E.A.J.F., Kuipers, J.A.M., 2020. Direct numerical simulation of a non-isothermal non-adiabatic packed bed reactor. Chem. Eng. J. 385, 123641.

Cheny, Y., Botella, O., 2010. The ls-stag method: a new immersed boundary/level-set method for the computation of incompressible viscous flows in complex moving geometries with good conservation properties. J. Comput. Phys. 229 (4), 1043–1076.

Das, S., 2017. Transport through bidisperse porous media: a multiscale modeling approach. PhD thesis. Chemical Engineering and Chemistry.

Das, S., Deen, N.G., Kuipers, J.A.M., 2017. Immersed boundary method (IBM) based direct numerical simulation of open-cell solid foams: hydrodynamics. AIChE J. 63 (3), 1152–1173.

Deen, N.G., Kriebitzsch, S.H.L., van der Hoef, M.A., Kuipers, J.A.M., 2012. Direct numerical simulation of flow and heat transfer in dense fluid–particle systems. Chem. Eng. Sci. 81, 329–344.

Dijkhuizen, W., 2008. Deriving closures for bubbly flows using direct numerical simulations. PhD thesis. University of Twente, Netherlands.

Ferziger, J.H., Kaper, H.G., 1973. Mathematical theory of transport processes in gases. Am. J. Phys. 41 (4), 601–603.

Franců, J., Mikyška, J., 2020. An alternative model of multi component diffusion based on a combination of the Maxwell-Stefan theory and continuum mechanics. J. Comput. Phys. 400, 108962.

Fuller, E.N., Schettler, P.D., Giddings, J.C., 1966. New method for prediction of binary gas-phase diffusion coefficients. Ind. Eng. Chem. 58 (5), 18–27.

Giovangigli, V., 1990. Mass conservation and singular multicomponent diffusion algorithms. Impact Comput. Sci. Eng. 2 (1), 73–97.

Giovangigli, V., 1991. Convergent iterative methods for multicomponent diffusion. Impact Comput. Sci. Eng. 3 (3), 244–276.

Goldstein, D., Handler, R., Sirovich, L., 1993. Modeling a no-slip flow boundary with an external force field. J. Comput. Phys. 105 (2), 354–366.

Hirschfelder, J.O., Curtiss, C.F., Bird, R.B., 1964. Molecular Theory of Gases and Liquids, 2nd printing. Wiley, New York.

Kempe, T., Fröhlich, J., 2012. An improved immersed boundary method with direct forcing for the simulation of particle laden flows. J. Comput. Phys. 231 (9), 3663–3684.

Kerkhof, P.J.A.M., Geboers, M.A.M., 2005. Analysis and extension of the theory of multi component fluid diffusion. Chem. Eng. Sci. 60 (12), 3129–3167.

Kim, D., Choi, H., 2006. Immersed boundary method for flow around an arbitrarily moving body. J. Comput. Phys. 212 (2), 662–680.

Krishna, R., Wesselingh, J.A., 1997. The Maxwell-Stefan approach to mass transfer. Chem. Eng. Sci. 52 (6), 861–911.

Kumar Das, S., 2019. General dusty gas model for porous media with a specified pore size distribution. Chem. Eng. Sci. 203, 293–301.

Kuo, K.K., 2005. Principles of Combustion, second edition. John Wiley and Sons, Inc.

Mason Edward, E.A., Malinauskas, A.P., 1983. Gas Transport in Porous Media: The Dusty-Gas Model.

Mazumder, S., 2006. Critical assessment of the stability and convergence of the equations of multi-component diffusion. J. Comput. Phys. 212 (2), 383–392.

Mittal, R., Iaccarino, G., 2005. Immersed boundary methods. Annu. Rev. Fluid Mech. 37 (1), 239–261.

Mittal, R., Dong, H., Bozkurttas, M., Najjar, F.M., Vargas, A., von Loebbecke, A., 2008. A versatile sharp interface immersed boundary method for incompressible flows with complex boundaries. J. Comput. Phys. 227 (10), 4825–4852.

Peerenboom, K.S.C., van Dijk, J., ten Thije Boonkkamp, J.H.M., Liu, L., Goedheer, W.J., van der Mullen, J.J.A.M., 2011. Mass conservative finite volume discretization of the continuity equations in multi-component mixtures. J. Comput. Phys. 230 (9), 3525–3537.

Peskin, C.S., 1972. Flow patterns around heart valves: a numerical method. J. Comput. Phys. 10 (2), 252–271.

Plasimo, 2024, https://plasimo.phys.tue.nl/.

Remick, R.R., Geankoplis, C.J., 1974. Ternary diffusion of gases in capillaries in the transition region between Knudsen and molecular diffusion. Chem. Eng. Sci. 29 (6), 1447–1455.

Saiki, E.M., Biringen, S., 1996. Numerical simulation of a cylinder in uniform flow: application of a virtual boundary method. J. Comput. Phys. 123 (2), 450–465.

Tadayon Mousavi, S., 2020. Modeling of Microwave Induced Plasmas — Application to the Production of Solar Fuels. PhD thesis. Eindhoven University of Technology, The Netherlands.

Taira, K., Colonius, T., 2007. The immersed boundary method: a projection approach. J. Comput. Phys. 225 (2), 2118–2137.

Tang, Y., Kriebitzsch, S.H.L., Peters, E.A.J.F., van der Hoef, M.A., Kuipers, J.A.M., 2014. A methodology for highly accurate results of direct numerical simulations: drag force in dense gas–solid flows at intermediate Reynolds number. Int. J. Multiph. Flow 62, 73–86.

Taylor, R., Krishna, R., 1993. Multicomponent Mass Transfer. Wiley.

Tenneti, S., Garg, R., Subramaniam, S., 2011. Drag law for monodisperse gas–solid systems using particle-resolved direct numerical simulation of flow past fixed assemblies of spheres. Int. J. Multiph. Flow 37 (9), 1072–1092.

Tseng, Y., Ferziger, J.H., 2003. A ghost-cell immersed boundary method for flow in complex geometry. J. Comput. Phys. 192 (2), 593–623.
Uhlmann, M., 2005. An immersed boundary method with direct forcing for the simulation of particulate flows. J. Comput. Phys. 209 (2), 448–476.
van Dijk, J., Peerenboom, K., Jimenez, M., Mihailova, D., van der Mullen, J., 2009. The plasma modelling toolkit plasimo. J. Phys. D, Appl. Phys. 42 (19), 194012.
Veldsink, J.W., Versteeg, G.F., van Swaaij, W.P.M., 1994. An experimental study of diffusion and convection of multicomponent gases through catalytic and non-catalytic membranes. J. Membr. Sci. 92 (3), 275–291.
Versteeg, H.K., Malalasekera, W., 2007. An Introduction to Computational Fluid Dynamics, the Finite Volume Method. Pearsoned.
Whitaker, S., 2009. Derivation and Application of the Stefan-Maxwell Equations. Revista Mexicana de Ingeniería Química.
Ye, T., Mittal, R., Udaykumar, H.S., Shyy, W., 1999. An accurate Cartesian grid method for viscous incompressible flows with complex immersed boundaries. J. Comput. Phys. 156 (2), 209–240.